



**HAL**  
open science

## Modeling and monitoring of foam propagation in highly permeable porous media under lateral water flow

Hossein Davarzani, Romain Aranda, Stéfan Colombano, Fabien Laurent,  
Henri Bertin

► **To cite this version:**

Hossein Davarzani, Romain Aranda, Stéfan Colombano, Fabien Laurent, Henri Bertin. Modeling and monitoring of foam propagation in highly permeable porous media under lateral water flow. *Advances in Water Resources*, 2022, 166, pp.104225. 10.1016/j.advwatres.2022.104225 . hal-03845515

**HAL Id: hal-03845515**

**<https://brgm.hal.science/hal-03845515>**

Submitted on 22 Jul 2024

**HAL** is a multi-disciplinary open access archive for the deposit and dissemination of scientific research documents, whether they are published or not. The documents may come from teaching and research institutions in France or abroad, or from public or private research centers.

L'archive ouverte pluridisciplinaire **HAL**, est destinée au dépôt et à la diffusion de documents scientifiques de niveau recherche, publiés ou non, émanant des établissements d'enseignement et de recherche français ou étrangers, des laboratoires publics ou privés.



Distributed under a Creative Commons Attribution - NonCommercial 4.0 International License

# Modeling and monitoring of foam propagation in highly permeable porous media under lateral water flow

Hossein Davarzani<sup>a</sup>, Romain Aranda<sup>a,b,c</sup>, Stéfan Colombano<sup>a</sup>, Fabien Laurent<sup>c</sup>, Henri Bertin<sup>b</sup>

a: BRGM, 3 Avenue Claude Guillemin, 45100, Orléans, France.

b: I2M, Université de Bordeaux, 33405, Talence, France.

c: Solvay RICL, 85 rue des Frères Perret, 69192, St Fons, France.

Email: h.davarzani@brgm.fr. Phone : +33 (0)2 38 64 33 52.

## Abstract

Foam injection is a promising option for soil remediation applications. However, predicting how it will propagate in highly permeable aquifers under groundwater flow is challenging. Here, we have studied pressure and saturation variations during foam propagation. A 2D tank packed with 1 mm glass beads was used to study foam injection in highly permeable porous media under lateral flow. Specifically, we evaluated the efficiency of pressure and time-domain reflectometer (TDR) sensors to predict foam propagation using an imaging technique. A numerical model coupling two-phase flow and surfactant transport was developed to simulate the experimental results. This model takes into account the effect of non-Newtonian behavior of foam, surfactant concentration, and critical capillary pressure through the definition of the mobility reduction factor (MRF). The experimental results show that the foam injection pressure first increases with a logarithmic law and then stabilizes. This pressure stabilization can be related to the state of pseudo-equilibrium between foam generation and destruction. We observed an asymmetrical foam propagation due to water lateral flow. Comparisons of the liquid saturation fields calculated by analysis of TDR probes and estimated by imaging show that the TDR sensors monitor foam propagation well in saturated porous media. They can predict the shape of the injected foam. Contrary to pressure sensors, it is possible to capture weak foam behavior using TDR sensors. Finally, the numerical model we have developed correctly captures the shape of foam propagation and its ability to divert water flows. This model produces the propagation of the strong foam well and predicts the saturation and pressure fields with good precision.

## Keywords

Non-Newtonian fluid, foam, monitoring, highly permeable porous media, 2D tank, numerical simulation

## Highlights

- Experimental and numerical studies of foam flow in highly permeable media
- Foam injection pressure stabilizes after balancing foam generation and destruction
- Pressure and time domain reflectometer sensors have the potential to monitor foam flow
- Time-domain reflectometers can capture the presence of strong and weak foam
- Model and experimental results agree well

## 1. Introduction

Foam injection technology has recently been used in porous media for contaminated-aquifer remediation processes. Varying the foam properties (liquid content, bubble size, viscosity, interfacial tension, capillarity) makes it suitable for different applications. As a blocking agent, it lowers the soil's relative permeability to water in highly permeable layers and diverts the fluid flow to lower permeability layers [Aranda et al., 2020; Bertin et al., 2017; Kovscek and Bertin, 2003; Omirbekov et al., 2020b]. Blocking foams can also be used to confine a contaminated area [Aranda et al., 2020; Omirbekov et al., 2020a; Portois et al., 2018]. Moreover, the injected treatment, using foam, can follow the highly permeable zone and leave the contaminants in the poorly permeable zones [Glass et al., 1988; Zhang et al., 2009] where the surfactant or traditional water-based amendment delivery techniques are not efficient because of the preferential flow. As a vectorization agent, foam can be used to transport additives and enhance redox reactions, additives such as chemicals [Zhong et al., 2011], gases [Maire et al., 2019], bacteria [Choi et al., 2009], and nanoparticles [Shen et al., 2011]. As a mobilization agent (“plug effect”), desorption foams can be used to desorb and push the pollutant towards a recovery well [Couto et al., 2009; Jeong and Corapcioglu, 2003; Longpré-Girard et al., 2016]. Its non-Newtonian behavior can mitigate the heterogeneity of the medium and improve remediation yield and rate. Therefore, remediation efficiency is increased in heterogeneous media.

Most porous media faced in soil contamination and remediation applications have a high permeability compared to those usually studied in petroleum reservoir engineering. Therefore, the application of foam flow to highly permeable porous media still faces specific challenges. In particular, its propagation and stability in highly permeable porous media under groundwater flow is still challenging. Contrary to foam flow in rock, in very highly permeable porous media foam flow depends on the bubble size. When the bubble size is much smaller than the pore size, foam behaves as a non-Newtonian, shear-thinning fluid. However, increasing the bubble size will drastically decrease the foam's apparent viscosity within a Newtonian behavior followed by a gradual transition to shear-thinning behavior for higher flow [Omirbekov et al., 2020a]. In this condition, foam flow occurs first with a weak foam regime and then with a strong foam flow regime [Aranda et al., 2020]. In the case of highly permeable porous media, it is recommended to inject the pre-generated foam using a finer porous media to increase the number of foam bubbles and, therefore, switch faster to the

strong regime flow with higher non-Newtonian behavior [Aranda et al., 2020; Omirbekov et al., 2020a].

Some authors have studied foam injection and propagation in experimental 2D tank setups. Most of these studies have focused on how heterogeneity and the presence of pollutant, or surfactant type and its concentration, influence foam behavior [Bertin et al., 2017; Bouzid et al., 2018; Forey et al., 2021; Longpré-Girard et al., 2016]. Longpré-Girard et al. (2016) used a small 2D tank to study foam application for mobility control and LNAPL recovery. They reported a better sweep indicating better mobility control using foam [Longpré-Girard et al., 2016]. Bertin et al. (2017) used a decimetric metallic 2D tank with two lateral glass panes to study foam flow in heterogeneous porous media. They showed that foam is generated in the high-permeability layer and will divert flow towards the low-permeability region [Bertin et al., 2017]. A 2D tank setup was used to study the delivery of an oxidant solution into the unsaturated layered porous media with success [Bouzid et al., 2018]. Forey et al. (2021) used a 2D tank equipped with absolute pressure sensors and imaging to study foam (reinforced with colloidal particles) formation and propagation in the presence of oil using a co-injection process. They found that solid silica particles can significantly reduce the destruction of foam in contact with oil. The interpolation of the pressure sensors allowed them to better analyze the foam formation and propagation [Forey et al., 2021]. More recently, Davarzani et al. (2021) performed a series of experiments on decimetric 2D tanks filled with 1 mm glass beads to investigate the blocking effect of foam for soil remediation applications. The pre-generated foam was injected at the bottom center of the tank. They observed the semi-circular propagation of the strong foam followed by an asymmetrical weak foam propagation around it. The presence of the weak foam means that only few lamellae are stable meaning in turn that resistance to flow is low in this zone. Moreover, they found that foam can completely divert the groundwater flow just after injection. However, the foam's stability depends significantly on the groundwater flow, mainly due to surfactant dilution in the water because of dispersion. The results showed that foam can also serve as a means for gas transport more homogeneously in porous media, especially for soil remediation applications [Davarzani et al., 2021].

Real-time in situ monitoring and modeling of how foam travels after injection into aquifers is needed to optimize the new remediation process using foam but still missing. Using pressure and time-domain reflectometry (TDR) sensors could fill this gap. Wu et al. (2012) tested three different cases of pure foam injection, foam injection into a silica sand column,

and foam injection into a column filled with sediment from a real site. They performed complex resistivity (electrical conductivity) and TDR measurements for all these cases in a centimeter-scale column. They reported the sensitivity of the electrical and TDR signal for monitoring foam flow in unsaturated porous media. TDR can capture increasing water content related to the presence of foam in the unsaturated zone. The authors concluded that TDR measurements are useful for estimating the water content, but they are not sufficiently sensitive to record the small changes in water redistribution at the pore scale [Wu et al., 2012]. Moreover, the presence of the air in unsaturated porous media can disturb the measurements of the TDR in the presence of the foam.

Turning to foam modeling, we see two main approaches to modeling flow in porous media [Zhang et al., 2009]: mechanistic (solve partial differential equations to compute foam texture) and empirical (modify the gas viscosity to calculate foam mobility).

The mechanistic approach uses bubble population balance models to accurately assess bubble formation, destruction, and propagation [Géraud et al., 2017]. The population-balance models are based on the definition of the number of lamellae as a variable coupled with the equation of two-phase flow in porous media. The gas mobility can be expressed as a function of the bubble density, water saturation, and other parameters. The dynamic change in foam texture can be captured in the unsteady-state regime. Many different existing formulations are developed to relate the foam viscosity (or gas mobility) to the bubble density. Kam and Rossen (2003) described bubble generation as a function of the time-averaged pressure gradient [Kam and Rossen, 2003]. Most population balance models are based on the lamella creation by the capillary snap-off [Bertin et al., 1998; Kavscek and Radke, 1994; Myers and Radke, 2000]. Ettinger and Radke (1992) used the same rate expression to describe the rate of bubble division, the second mechanism for creating foam [Ettinger and Radke, 1992]. Recently, Almajid et al. (2021) developed a mechanistic model with the constitutive relation depending on the local pressure gradient, permeability, and bubble density coming from the pore-scale flow properties [Almajid et al., 2021]. This can model low- and high-quality regimes in porous media. Many other models have been developed to simulate foam flow in porous media like the bubble population-balance model [Falls et al., 1988; Fergui et al., 1998; Kavscek and Radke, 1994]), the fractional flow theory [Zhang et al., 2009], the catastrophe theory [Kam, 2008], the percolation theory models [Rossen, 1990] and filtration theory [Wan et al., 2001]. Most of these models simulate the phenomenon at a pore-scale and need a lot of computer power. They are useful at small scale to understand the mechanisms and their

dependence on some parameters but are difficult to use at the field scale. The complexity of the mechanistic model is not necessary if it is known that strong foam will be created [Kam et al., 2007]. The fractional flow model is not suitable for some foam flows due to the number of assumptions needed [Zhang et al., 2009]. Moreover, it is difficult to obtain the model parameters from experimental data because of the extrapolation needed.

Empirical models represent the mechanisms of foam formation and destruction on a macroscopic scale and require few parameters compared to mechanistic models such as the population balance models. A mobility reduction factor (MRF) is used to adjust the gas mobility related to foam generation and destruction. Some studies focused on modifying only the gas viscosity to drive foam mobility. They consider the effect of surfactant concentration, water saturation, gas velocity [Marfoe, 1987], or oil saturation [Chang et al., 1990; Islam, 1988] on the foam apparent viscosity. Mohammadi et al. (1995) proposed to modify the gas relative permeability to derive foam mobility depending on the surfactant concentration and pressure gradient [Mohammadi et al., 1995].

In porous media, capillary pressure is a key element in determining foam texture. Foam texture includes descriptions of bubble size, shape, and distribution. Khatib et al., 1988 have experimentally shown that there is a transition from strong foam to weak foam at a critical capillary pressure  $p_c^*$  [Khatib et al., 1988]. It is also possible to link this critical capillary pressure to a critical saturation. The value of the critical saturation depends on several parameters such as the permeability of the porous medium, the surfactant type, and its concentration or the nature of the fluid surrounding the foam. This value must therefore be measured experimentally. When the pressure exceeds the critical capillary pressure  $p_c^*$ , it is assumed that the foam is destroyed, drastically affecting its mobility. A steady-state model for the foam-water system called the fixed- $p_c^*$  model was developed by Zhou and Rossen, (1995) where the limiting capillary pressure is independent of gas and liquid flow [Zhou et al., 1995]. In this model, the gas mobility at critical capillary pressure  $p_c^*$  is a function of the foam quality and the critical water saturation. Rossen et al., (1999) extended the fixed- $p_c^*$  model to calculate MRF taking into account the surfactant concentration and this critical saturation [Rossen et al., 1999]. Cheng et al., (2000) modified the proposed equation to include the non-Newtonian behavior of foam according to gas flow rate [Cheng et al., 2000]. This model was modified by Dholkawala, (2007), adding the phenomenon of foam generation and coalescence [Dholkawala et al., 2007]. The reader can look at [Hematpur et al., 2018; Zhang et al., 2009]

for a detailed formulation of the different foam flows in porous media models and their comparisons.

The best way to model foam flow depends on the available experimental data, objectives, and available modeling tools. As the phenomena studied in this work are at the Darcy scale and due to the weaknesses of fractional flow theories, we propose an empirical MRF model with mechanistic generalized Darcy's law to simulate foam flow in porous media. Here, the MRF model was built upon an existing empirical approach used by [Cheng et al., 2000] considering the effect of the non-Newtonian behavior, surfactant concentration, and critical capillary pressure on the foam flow mobility. The main advantage of this empiric model for calculating the MRF is needing fewer physical fitting parameters compared to a population balance-based model taking into account the most important physical phenomena influencing foam mobility. Surfactant concentration plays a crucial role in foam stability and also in the MRF value [Wang et al., 2012]. Therefore, it is essential to take into account surfactant transport when modeling foam flow in porous media. The surfactant transport in porous media is modeled using the diffusion and advection equations taking into account the dispersion. The velocity field for the advection term comes from the solution of Darcy's law. Gas mobility in Darcy's law is also a function of the surfactant concentration. We propose, therefore, a strongly coupled model.

Our work gives a better understanding of foam flow in highly permeable aquifers using experimental and numerical approaches. The main focus was on pressure and saturation variations during foam propagation. A meter-scale 2D tank setup filled with 1 mm glass beads was used to model foam injection in highly permeable porous media. This 2D tank is a larger and improved version of that described in [Davarzani et al., 2021]. With the large-scale 2D tank used in this study, we could better investigate foam propagation. The setup gave us the saturation directly from the imaging thanks to the transparent glass of the tank front. The pressure and TDR sensor network proposed in this new 2D tank, installed in the rear, measured water saturation and pressure. The experimental data obtained in this study was used to evaluate the potential of TDR and pressure gauges as tools for monitoring foam injection in the saturated zone. The lack of gas in this zone can help to better evaluate the presence of the foam and how it flows in porous media. Comparing these with saturation fields obtained using imaging can help to better assess the potential of other monitoring techniques. The saturation (using the TDR sensors and imaging technique) and pressure data can be then served to validate the model results. The water flow was generated horizontally to

model a more realistic foam injection case in the aquifer. The pre-generated foam was injected at the bottom center of the tank. To our knowledge, there is a lack of knowledge in the literature concerning the study of foam flow under water flow in a metric-scale 2D setup. A numerical model, coupling two-phase (foam and water) flow and surfactant transport, was developed using Comsol Multiphysics® to simulate the experimental results.

## 2. Theoretical consideration and numerical model formulation

The mathematical formulations we used to simulate foam flow in porous media are as follows. We used Wang's mixture model [Wang and Beckermann, 1993] coupled with an empirical model to represent foam mobility. The solute transport equations were used to simulate surfactant transport during foam injection. This choice was motivated by the fact that we studied the problem at the two-dimensional Darcy scale. The mixture model is the simplest to be solved numerically because the coupling between the equations is not strong.

### 2.1. Two-phase flow formulation

The conservation of the mass of the mixture can be written as

$$\phi \frac{\partial \rho}{\partial t} + \nabla \cdot (\rho \mathbf{u}) = 0 \quad (1)$$

where  $\mathbf{u}$  is the mixture Darcy's velocity ( $\text{m}\cdot\text{s}^{-1}$ ),  $\phi$  porosity, and  $\rho$  ( $\text{kg}\cdot\text{m}^{-3}$ ) is the mixture density calculated as below

$$\rho = S_w \rho_w + S_{nw} \rho_{nw} \quad (2)$$

$$\rho \mathbf{u} = \rho_w \mathbf{u}_w + \rho_{nw} \mathbf{u}_{nw} \quad (3)$$

where  $S_i$ ,  $u_i$ , and  $\rho_i$  are the fluid saturation, velocity, and density of  $i = w, nw$  phase, respectively. The mean dynamic viscosity of the two-phase mixture ( $\text{Pa}\cdot\text{s}$ ) is defined as

$$\mu = \frac{\rho}{\frac{\rho_w k_{r,w}}{\mu_w} + \frac{\rho_{nw} k_{r,nw}}{\mu_{nw}}} \quad (4)$$

where  $k_{r,i}$  refers to the relative permeability of phase  $i$  ( $w, nw$ ).

To handle these physical quantities more easily, the relative mobility  $\lambda_{r,i}$  of phase  $i$  is defined as

$$\lambda_{r,i} = \mu \frac{k_{r,i}}{\mu_i}, \text{ with } i = w, nw \quad (5)$$

$$\lambda_{r,w} + \lambda_{r,nw} = 1 \quad )$$

Darcy's two-phase flow equations for isotropic porous media can be written as below

$$\mathbf{u}_i = -\frac{\mathbf{K}_{int} k_{r,i}}{\mu_i} \cdot (\nabla p_i - \rho_i \mathbf{g}), \text{ with } i = w, nw \quad (6)$$

where  $\mathbf{K}_{int}$  ( $\text{m}^2$ ) refers to the intrinsic permeability tensor, which can be reduced to a scalar permeability  $K_{int}$  ( $\text{m}^2$ ) for an isotropic medium.  $\mathbf{u}_i$  ( $\text{m}\cdot\text{s}^{-1}$ ) is the Darcy velocities of phase  $i$ ,  $\mu_i$  ( $\text{Pa}\cdot\text{s}$ ) the fluid dynamic viscosity,  $p_i$  ( $\text{Pa}$ ) its pressure,  $\rho_i$  ( $\text{kg}\cdot\text{m}^{-3}$ ) its density,  $\mathbf{g}$  ( $\text{m}\cdot\text{s}^{-2}$ ) the standard gravitational acceleration. The pseudo mixing pressure which was formulated by [Chavent, 1976] reads

$$\nabla p = \lambda_{r,w} \nabla p_w + \lambda_{r,nw} \nabla p_{nw} \quad (7)$$

Then we can deduce the mixture Darcy's law as

$$\mathbf{u} = -\frac{K_{int}}{\mu} [\nabla p - \rho_k \mathbf{g}] \quad (8)$$

where  $\rho_k$  ( $\text{kg}\cdot\text{m}^{-3}$ ) the kinetic density of the mixture that is defined by

$$\rho_k = \lambda_{r,w} \rho_w + \lambda_{r,nw} \rho_{nw} \quad (9)$$

The mass balance related to the wetting saturation phase,  $S_w$  becomes

$$\frac{\partial(\phi S_w \rho_w)}{\partial t} + \nabla \cdot [\lambda_w \rho \mathbf{u}] = \nabla \cdot \left[ D_c \nabla S_w - \frac{\rho K_{int}}{\mu} \lambda_w \lambda_{nw} \Delta \rho \mathbf{g} \right] \quad (10)$$

where  $D_c$  ( $\text{Pa}\cdot\text{s}$ ) is the capillary diffusion coefficient defined as

$$D_c = -\frac{\rho K_{int}}{\mu} \lambda_w \lambda_{nw} \frac{\partial p_c}{\partial S_w} \quad (11)$$

Since the porosity is constant and the two immiscible fluids jointly fill the void space, the sum of the phase saturations must be equal to one

$$S_w + S_{nw} = 1 \quad (12)$$

The effective wetting saturation is usually defined as

$$Se_w = \frac{S_w - S_{r,w}}{1 - S_{r,w}} \quad (13)$$

where  $S_{r,w}$  (-) is the residual wetting phase saturation. The difference between the non-wetting and wetting pressure is known as the capillary pressure and can be defined as a function of the normalized wetting fluid saturation

$$p_c(Se_w) = p_{nw} - p_w \quad (14)$$

We used the van Genuchten-Mualem model to relate the capillary pressure and relative permeability to the wetting phase saturation [Mualem, 1976; van Genuchten, 1980]

$$Se_w = (1 + (\alpha p_c)^n)^{-m} \quad (15)$$

where  $\alpha$  ( $m^{-1}$ ) and  $n$  are the van Genuchten soil parameters with  $m = 1 - 1/n$ . The relative permeability for the wetting and non-wetting phase can be written, respectively, as

$$k_{r,w} = Se_w^l \left(1 - (1 - Se_w^{1/m})^m\right)^2 \quad (16)$$

$$k_{r,nw} = (1 - Se_w)^l (1 - Se_w^{1/m})^{2m} \quad (17)$$

The parameter  $l$  has been considered equal to 0.5, which is commonly accepted in this type of porous medium [Chen et al., 1999; Mualem, 1976]. Equation (10) describes the two-phase flow in association with the equation for conservation of the mass of the mixture, Equation (1), with three unknowns.  $S_w$ ,  $p$ , and  $p_c$ . The system is closed thanks to the constitutive relationships for the capillary pressure and relative permeability (Equations 12-17).

Using the definition of pseudo mixing pressure, equation (7), and the definition of capillary pressure, it is possible to calculate the pressure gradients of each phase as below

$$\nabla p_w = \nabla p - \lambda_{r,nw} \nabla p_c \quad (18)$$

$$\nabla p_{nw} = \nabla p + \lambda_{r,w} \nabla p_c \quad (19)$$

Once the governing equations related to the two-phase flows in porous media have been established, we must model the behavior of the foam in porous media. The following hypotheses are necessary to model foam flow at the Darcy-scale: i) foam is considered as a single gas phase [Zhou et al., 1995], ii) the mobility of water depends on the water saturation, whether or not there is foam [Zhou et al., 1995], and finally, iii) the mobility of the gas is controlled by the texture of the foam [Falls et al., 1989].

Foam has a high viscosity that varies depending on how it is generated and destroyed. It is therefore necessary to integrate these properties into the equations. Thus, the foam will not be modeled as a two-phase structure, but as a single non-wetting phase affected by a variable mobility reduction factor (MRF) modifying the phase mobility. In the equations, the wetting phase will represent only the water around the foam and not the surfactant solution that is part of the foam. The gas-phase of the foam is considered continuous and the effect of the lamellae is presented by the MRF. The MRF is applied to the gas mobility to obtain that of the foam as

$$\lambda_{fm} = \frac{\lambda_g}{MRF} \quad (2)$$

where  $\lambda_{fm}$  is foam mobility ( $\text{Pa}^{-1} \cdot \text{s}^{-1}$ ) and  $\lambda_g$  gas mobility ( $\text{Pa}^{-1} \cdot \text{s}^{-1}$ ).

The resistance factor (RF) represents the reduction in foam mobility compared to a single-phase flow of water. Therefore, the two factors are related as

$$MRF = RF \times \frac{\mu_w}{\mu_g} \quad (21)$$

MRF is determined experimentally from foam flow in porous columns. It is known to depend on several parameters such as porous media petro-physical properties, surfactant type and concentration, and flow condition. It is a commonly used key parameter that determines the foam flow regime in porous media. The MRF can vary from a few tens for foams with a coarse texture (weak foam) to hundreds of thousands for foams with a fine texture [Lee, 2014]. The case where  $MRF = 1$  corresponds to a conventional gas-phase flow without foam.

Here, we considered that the MRF varies as a function of the multiplication of the maximum mobility reduction and different factors that vary between 0 and 1. This concept has been successfully widely used in different commercial reservoir simulators such as

STARS (CMG), ECLIPS (Schlumberger company), and UTCHEM (University of Texas at Austin).

## 2.2. Surfactant transport formulation

Solute transport is governed by the classic differential advection-dispersion equation in porous media

$$\frac{\partial(\phi S_w c)}{\partial t} + \mathbf{u} \cdot \nabla c - \nabla \cdot (\mathbf{D}_{eff} \cdot \nabla c) = Q_s \quad (22)$$

where  $c$  is the surfactant concentration ( $\text{mol} \cdot \text{m}^{-3}$ ),  $\mathbf{D}_{eff}$  the effective diffusion coefficient tensor ( $\text{m}^2 \cdot \text{s}^{-1}$ ),  $\mathbf{u}$  the mixture Darcy velocity field ( $\text{m} \cdot \text{s}^{-1}$ ), and  $Q_s$  ( $\text{mol} \cdot \text{m}^{-3} \cdot \text{s}^{-1}$ ) a sink or source term. Since AOS is anionic, it is assumed that adsorption is negligible on glass beads ( $Q_s = 0$ ).

The effective diffusion coefficient tensor includes the contributions of molecular diffusion and hydrodynamic dispersion by the effect of flow velocity. The values of the effective diffusion coefficient tensor depend on the solute transport regime. To evaluate this regime, it is necessary to calculate the Péclet number as

$$Pe = \frac{d_p u}{D_m} \quad (23)$$

where  $d_p$  is the pore mean size of the porous media (m),  $D_m$  is the molecular binary diffusion coefficient of AOS ( $\text{m}^2 \cdot \text{s}^{-1}$ ) in water, and  $u$  ( $\text{m} \cdot \text{s}^{-1}$ ) the infiltration velocity.

The Péclet number for a water flow applied in this study is in the order of  $\cong 10^2$ . This Péclet value shows that the pure mechanical dispersion phenomenon ( $300 < Pe < 10^5$ ) is dominant. Therefore, a classical expression was used to calculate the longitudinal and transversal dispersion coefficients [Delgado, 2007]:

$$\frac{D_{eff,L}}{D_m} = \frac{1}{\tau} + 1.8Pe \quad (24)$$

$$\frac{D_{eff,T}}{D_m} = \frac{1}{\tau} + 0.025Pe \quad (25)$$

where  $D_{eff,L}$  and  $D_{eff,T}$  are the longitudinal and transversal dispersion coefficients ( $\text{m}^2 \cdot \text{s}^{-1}$ ), respectively.  $\tau$  is the tortuosity of the medium, estimated by the Millington and Quirk

relationship in a saturated medium [Millington and Quirk, 1961]:

$$\tau = \phi^{-1/3} \quad (26)$$

The molecular diffusion coefficient of AOS was deduced from [Azmi et al., 2019; Movchan et al., 2015; Wang et al., 2017] and we suggest an average value of  $D_m = 10^{-10} \text{ m}^2 \cdot \text{s}^{-1}$ .

### 3. Experimental study

#### 3.1. Materials and fluids

We used 1 mm glass beads to fill the 2D tank. The main reason is that the same type and size of glass beads were used in our previous studies [Aranda et al., 2020; Omirbekov et al., 2020a; Omirbekov et al., 2020b]. The measured permeability and porosity of porous media made of these glass beads were  $8.4 \times 10^{-10} \text{ m}^2$  and 0.37. Using beads made of glass means good transparency properties and better visualization of flows and saturation by imaging.

Following the results in [Aranda et al., 2020; Omirbekov et al., 2020a; Omirbekov et al., 2020b] we used a solution of alpha-olefin sulfonate surfactant (AOS) concentrated at 4×CMC for the experiments.  $\text{N}_2$  (purity > 99.99%) and carbon dioxide (purity > 99.7%) were used to generate the foam and reduce the air trapping in the porous column, respectively.

#### 3.2. Experimental setup and procedure

##### 3.2.1. Foam generator and 2D tank setup

The experimental setup is presented in Figure 1. This setup includes a porous column to generate foam. The pre-generated foam is then injected into the center bottom of a 2D tank filled with glass beads and saturated with water.

We used a PVC column (10 cm long) filled with very fine glass beads (0.1 mm diameter) to generate foam. This generates a stronger foam with a sharper interface than foam generated using a co-injection technique [Aranda et al., 2020]. The permeability and porosity of this porous column were  $1.1 \times 10^{-11} \text{ m}^2$  and 0.38, respectively. The AOS surfactant solution and  $\text{N}_2$  gas were co-injected, using a Tee connector, into the pre-generator to generate foam. We used a mass flow controller (Brooks Delta Smart II;  $\pm 0.7\%$  of rate and  $\pm 0.2\%$  F.S.) to control the gas flow. The volume of the surfactant solution was regulated using a peristaltic pump (Ismatec Reglo ICC;  $\pm 1\%$  reading).

The 2D tank (length=1 m, height=0.6 m, and width=0.085 m) is composed of a central porous reservoir and two side cavities (Figure 1). The front part of the 2D tank is made of transparent glass to photograph the foam flow using the light reflected method. That transparent glass also allowed us to visualize using photography. The rear of the tank was made with a special polymer to plug a network of pressure and TDR (time domain reflectometry) sensors. Time-domain reflectometry is the most widely used non-destructive method to determine the water content of porous media.

The cavities are separated from the central reservoir using a perforated metal plate. The cavities distribute pressure homogeneously across the cavities. Foam is injected from a center bottom hole (3.125 cm); five side connection points help to generate the lateral water flow. Given the tank depth and the size of the foam inlet, small 3D effects near the nozzle may occur, but Philippe et al. (2021), using a smaller 2D tank, have shown that this effect can be neglected even for a less stable two-phase flow [Philippe et al., 2021].

We followed the same experimental protocol as [Davarzani et al., 2021] and as shown in Figure 1. We used a primary circuit to inject foam from the bottom. The secondary and tertiary circuits were used to create the lateral flow of water and to pump out excess water from the cavities, respectively. Two absolute pressure sensors (Keller<sup>®</sup> PA-33X; accuracy:  $\pm 1.5$  Pa) were placed upstream of the pre-generator. All circuit pipes were made of PVC and had an inside diameter of 1/4 inch.

We used the secondary circuit to inject deionized water into the left cavity using a peristaltic pump (Ismatec<sup>®</sup> Reglo ICC). We injected water at two points into the cavity to obtain a more homogeneous lateral flow. Two other pipes were used to pump water from the right-side cavity. These two pipes were installed at the same level as the left cavity's pipes. The pumping and injection flow rates were the same in all pipes to ensure a homogeneous and constant lateral flow.

After injecting foam through the central hole, the water level inside the tank increased. To keep the water level constant, the excess water was pumped using two pipes (tertiary circuit) installed in each cavity at the saturated zone surface. The pumped water weight was measured using a mass balance (Sartorius<sup>®</sup> MSE8201S; precision:  $\pm 0.1$  g). From this, we calculated the volume of foam injected into the 2D tank.

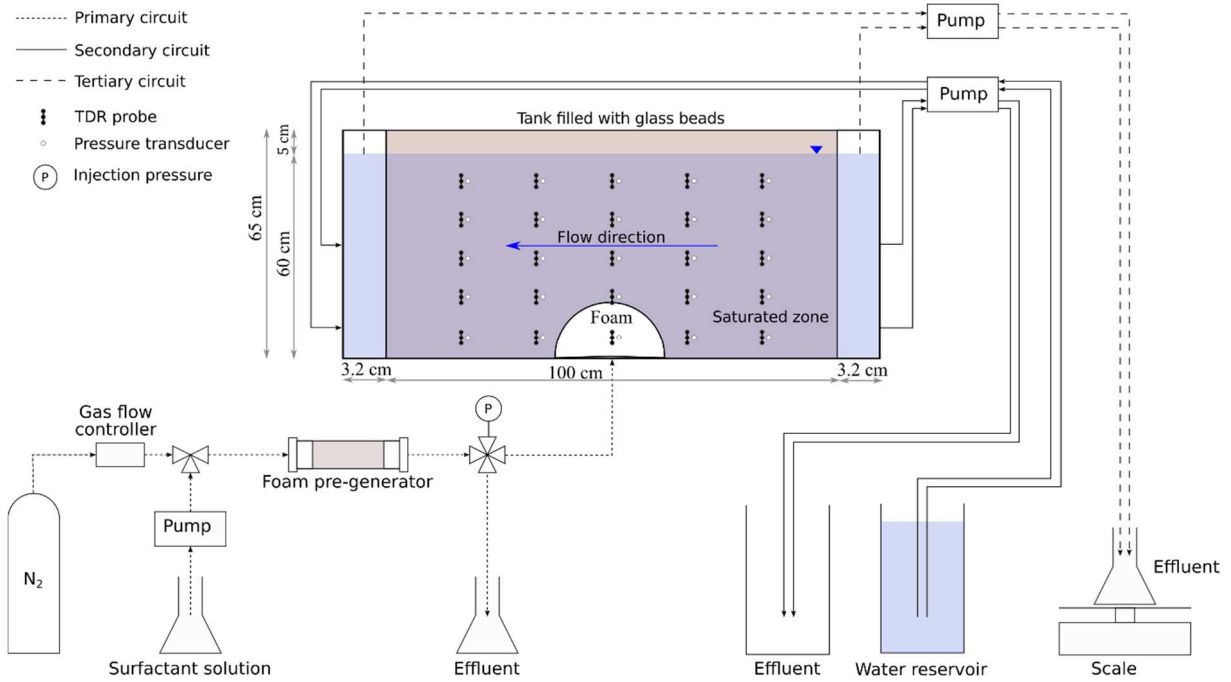


Figure 1 Back view of the experimental setup for foam injection in highly permeable porous media using a foam pre-generated column. A 2D tank was filled with 1 mm glass beads. The water flows horizontally; pre-generated foam is injected from a bottom center hole. Time-domain reflectometer (TDR) probes indirectly measure the water saturation and the pressure transducers measure the pressure.

We used a photography system installed in a darkroom. This system includes a high-resolution camera of 45.7 megapixels of brilliant resolution with a 105 mm focal length lens, and a spotlight to photograph the foam injection process installed in a darkroom. A standard grey-scale that was attached to the tank surface allowed the images to be calibrated.

A set of 25 TDR probes and 25 absolute pressure sensors are inserted in the back part of the tank to measure the saturation and pressure fields inside the porous media in the 2D tank. TDR devices are electronic and transmit the wave by two parallel embedded metal rods (waveguides). These waveguides are connected to the TDR via a coaxial cable. TDR works based on the travel time of high-frequency electromagnetic signals into the medium. The dielectric permittivity of the medium is then calculated using the reflected signals. Dielectric permittivity is a physical property that characterizes the degree of electrical polarization of material under the influence of an external electric field. A TDR device directly measures the relative permittivity, which is defined as the ratio of the real effective dielectric permittivity and the free space permittivity. Relative permittivity is the ability of a material to obtain intrinsic polarization. The TDR probes used for this device were ECH<sub>2</sub>O 5TE manufactured by METER-Group ( $\pm 1$  from 1 to 40,  $\pm 15\%$  measurement from 40 to 80) with dimensions of 10 cm $\times$ 3.2 cm (waveguides 5 cm long and 0.5 cm wide) and a range between 1 (air) to 80

(water). These probes use a wave of frequency 70 MHz and the value of the relative permittivity measured corresponds to an average over a square mesh with 5 cm sides, centered on the probe. The complex dielectric permittivity consists of two parts, a real and an imaginary part. However, at high frequencies, the imaginary part is negligible [Glover, 2015; Heimovaara et al., 1994]. The permittivity of a porous medium is strongly related to polar molecules like water due to electric polarization and dipolar polarization of the water molecule. The relative permittivity (dielectric constant) of water is about 80, while most of the soil particles have relative permittivity values between 2 and 7, and that of air is equal to 1. Consequently, the relative permittivity of porous media can be used to estimate the water saturation. The TDR device should be calibrated to determine the relationship between the measured porous media's effective relative permittivity and the water saturation. The existing empirical formulations can also be used to estimate the water saturation in some cases using empirical relationships (e.g., [Topp et al., 1980]) or theoretical models such as the complex refractive index model (CRIM) [Birchak et al., 1974; Endres and Knight, 1992; Roth and Attinger, 1990].

The absolute pressure sensors are of the Keller PR-21 Y type with an accuracy of  $\pm 7.5$  mbar. The locations of the probes in the 2D tank are shown in Figure 2. The first and second digits of the sensor name correspond to its row counting from the top of the tank and its column starting from the left of the tank, respectively.

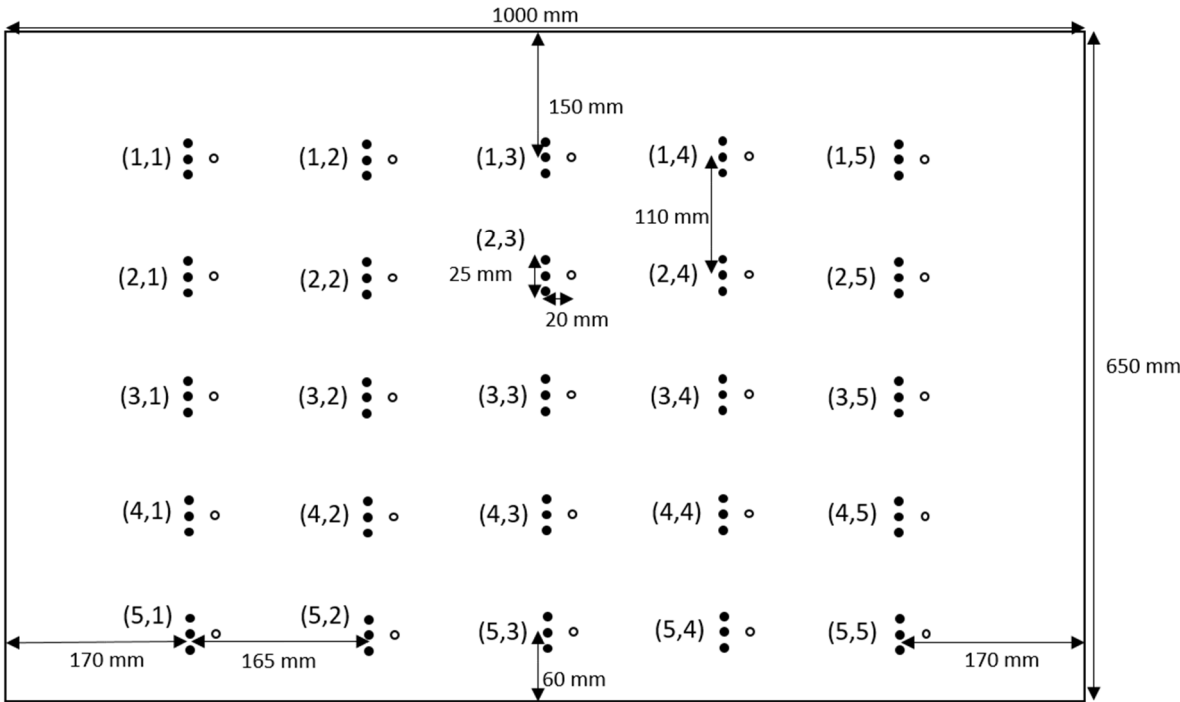


*Figure 2 Locations of pressure sensors and TDR probes on the 2D tank. TDR probes and pressure sensors are represented by three black dots and a white dot, respectively.*

### **3.2.2. Experimental procedures**

The 2D tank was filled up completely with 1 mm glass beads. Deionized water was then injected through the center bottom injection point with a very low flow rate (2.0 mL/min). This low flow rate injection ensures stable water flow upward and avoids air being trapped in pores. We left a small unsaturated zone in the 2D tank to avoid any water spill from the top (see Figure 1). A lateral flow of 1.4 m/day was created using the secondary circuit. A blue dye was injected from the left cavity to verify the homogeneity of the lateral flow.

The foam generator was first filled with 0.1 mm glass beads. To avoid any air trapping, CO<sub>2</sub> was injected before injecting water and then surfactant ( $C_s = 4 \times \text{CMC}$ ) into the column.

Finally, N<sub>2</sub> gas and the surfactant solution were co-injected into the column with a foam quality of 85% and a total flow rate of 4 mL/min. As soon as we observed the strong foam at the column outlet and the pressure signal before the foam generator becomes stable, the foam was directed to the 2D tank. At the same time, the tertiary pipes evacuated any water excess before and during the experiment. Photographs were also taken before and during the foam injection. Permittivity and pressure values were recorded every 30 s using a Campbell Scientific data logger CR6.

## **3.3. Data Analysis**

### **3.3.1. Image analysis**

We used light reflection methods (LRM) (see [Alazaiza et al., 2016]) to obtain the relationship between light intensity and liquid saturation. A linear relationship between the optical density and liquid saturation in foam can be considered [Davarzani et al., 2021].

$$S_w = \alpha OD + \beta \quad (27)$$

where coefficients  $\alpha$  and  $\beta$  are then calculated from two calibration images where the saturations are known. We used an image of foam zone near the injection point ( $S_w = 0.05$ ) and a second image before foam injection ( $S_w = 1$ ) to find these coefficients' values.

The transmitted light can be related to the sum of the measured reflected light intensity  $I_r$ , and the light intensity reflected by a perfectly white surface  $I_i$  [Flores et al., 2011; Kechavarzi et al., 2000; Schincariol et al., 1993; Stimson, 1974].

$$OD = -\log_{10} \left( \frac{I_r}{I_i} \right) \quad (28)$$

Once the saturation was calculated, all meshes were colored according to their gray intensity. Then the intensity and saturation fields could be discretized. The saturation slices of [0; 0.1], [0.1; 0.3], [0.3; 0.5], [0.5; 0.7], [0.7; 0.9], [0.9; 1] were selected and a color-scale linked the saturation values to a range of color from white to blue. For more details on image analysis, the reader can refer to [Davarzani et al., 2021] for foam flow and [Colombano et al., 2020; Colombano et al., 2021; Luciano et al., 2010; O'Carroll et al., 2004; Philippe et al., 2020; Philippe et al., 2021] for non-aqueous phase liquid flow.

### 3.3.2. TDR data acquisition and calibration

In this study, an empirical relationship was used to obtain the water content  $\theta_w$  from the relative permittivity data [Topp et al., 1980]

$$\varepsilon^*(\theta) = 3.57 + 31.7\theta + 114\theta^2 - 68.2\theta^3 \quad (29)$$

where  $\theta$  is the volumetric liquid content [-] and  $\varepsilon^*$  the relative permittivity of the bulk system measured using a TDR sensor [-]. By performing a 3rd order polynomial regression on the inverse of this function for  $\theta_w \in [0; 0.4]$ , we get ( $R^2 = 0.9998$ ).

$$\theta_w(\varepsilon^*) = 1.06 \times 10^{-5} \varepsilon^{*3} - 7.54 \times 10^{-4} \varepsilon^{*2} + 2.95 \times 10^{-2} \varepsilon^* - 9.11 \times 10^{-2} \quad (30)$$

Each probe was then calibrated independently by performing a linear relationship from two measurements where the liquid content is known:  $\theta = 0$  (dry porous medium) and  $\theta = \phi$  (porous medium saturated with water). Since the values depend on the arrangement of the glass beads, this calibration was done before each experiment.

## 4. Results and Discussions

### 4.1. Experimental results demonstration

This section discusses how pressure changes at the injection point, and the pressure and saturation fields. The saturation fields measured by TDR are compared with those estimated using image analysis.

#### 4.1.1. Injection pressure

The foam was injected under the same conditions throughout the experiment. Figure 3 shows how injection pressure changes as a function of time. We observed a steady increase in pressure followed by signal stabilization. This phenomenon can be explained in two complementary ways: aging of the foam at the level of the displacement front which causes a local decrease in the apparent viscosity, and a reduction in water saturation at the level of the injection zone which leads to an increase in local capillary pressure to its critical value.

If we consider that the aging of the foam at the level of the displacement front is weak, then from measuring the pressure field we can evaluate the critical capillary pressure. This depends on the formulation of the foam, its quality, and the properties of the porous medium. Since all of our experiments were carried out with the same parameters, it is possible to deduce the critical capillary pressure  $p_c^*$  as

$$p_c^* = p_{foam}^* - p_l \quad (31)$$

where  $p_{foam}^*$  is the stabilizing pressure of the foam during the experiments and  $p_l$  is the pressure of the liquid, depending on the hydrostatic pressure in the tank because there is no water flow at the injection level. Thus, it is possible to conclude that the critical capillary pressure of this foam in a porous medium of 1 mm glass beads is approximately 195 mbar. This value is in the same order of magnitude found in the literature for unconsolidated porous media [Khatib et al., 1988].

During the early stages of the injection, the pressure development follows a logarithmic law (see Figure 3). This is the behavior that should be observed in the case of the injection of a viscous fluid, together with propagation in the form of a perfect half-disk. These measurements are therefore in agreement with the observations showing that the shape of the strong foam is a half-disk.

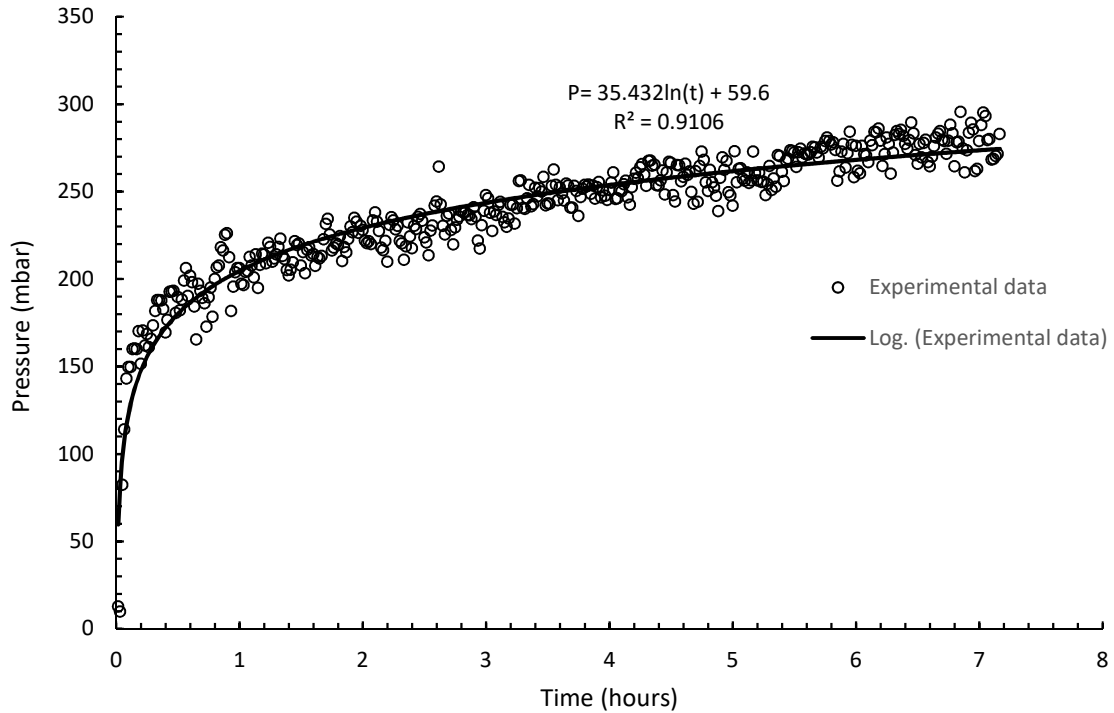


Figure 3 Evolution of pressure of foam injection in the 2D tank injection point. The pressure evolution follows a logarithmic law.

#### 4.1.2. Saturation and pressure fields

Figure 4 shows how the liquid saturation changes over time on line 3 of the TDR probes. Line 3 contains five TDR probes and is in the middle of the tank. Values greater than 1 and less than 0 are due to measurement accuracy, which is around  $\pm 0.1\%$  for the saturation related to the permittivity measurement precision ( $\pm 1$ ). The initial permittivity values (glass beads fully saturated by water) were varied between 16 and 20 according to the position of the sensors in the 2D tank and could fall to a value close to 3 (e.g. for sensor (5,3)) after foam injection.

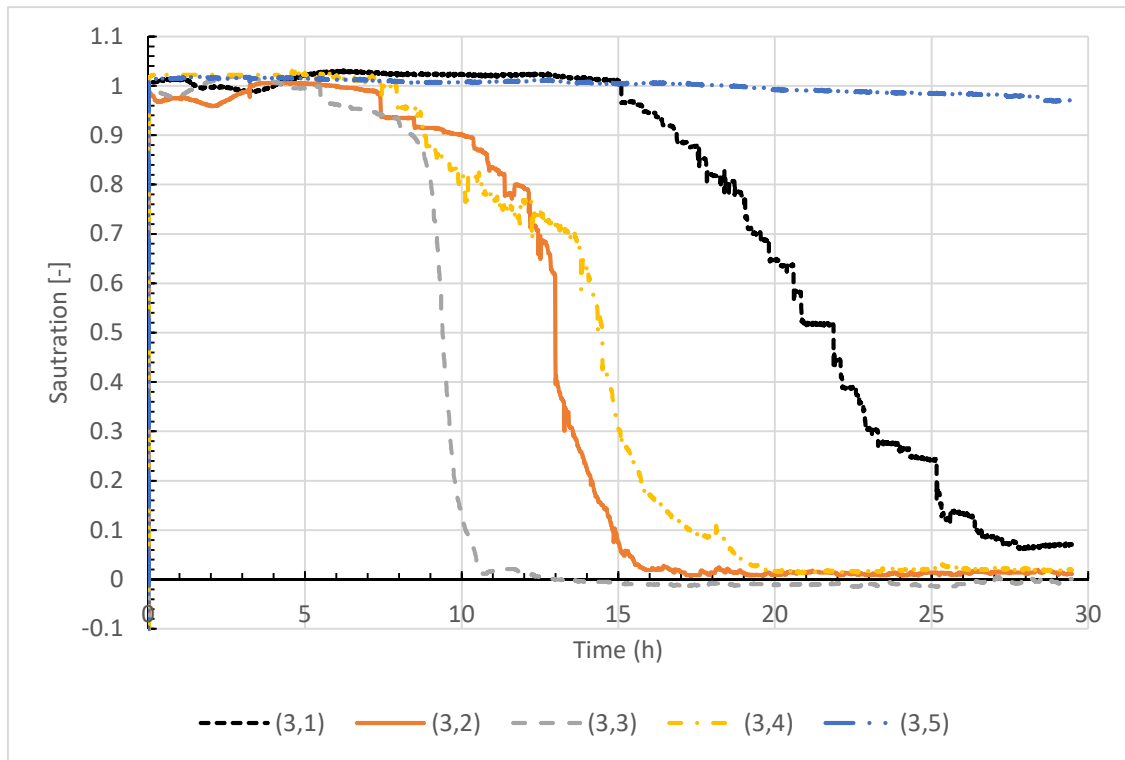


Figure 4. Changes in liquid saturation as a function of time on line 3 of the 2D tank. Water saturations were deduced from the relative permittivity values measured using TDR.

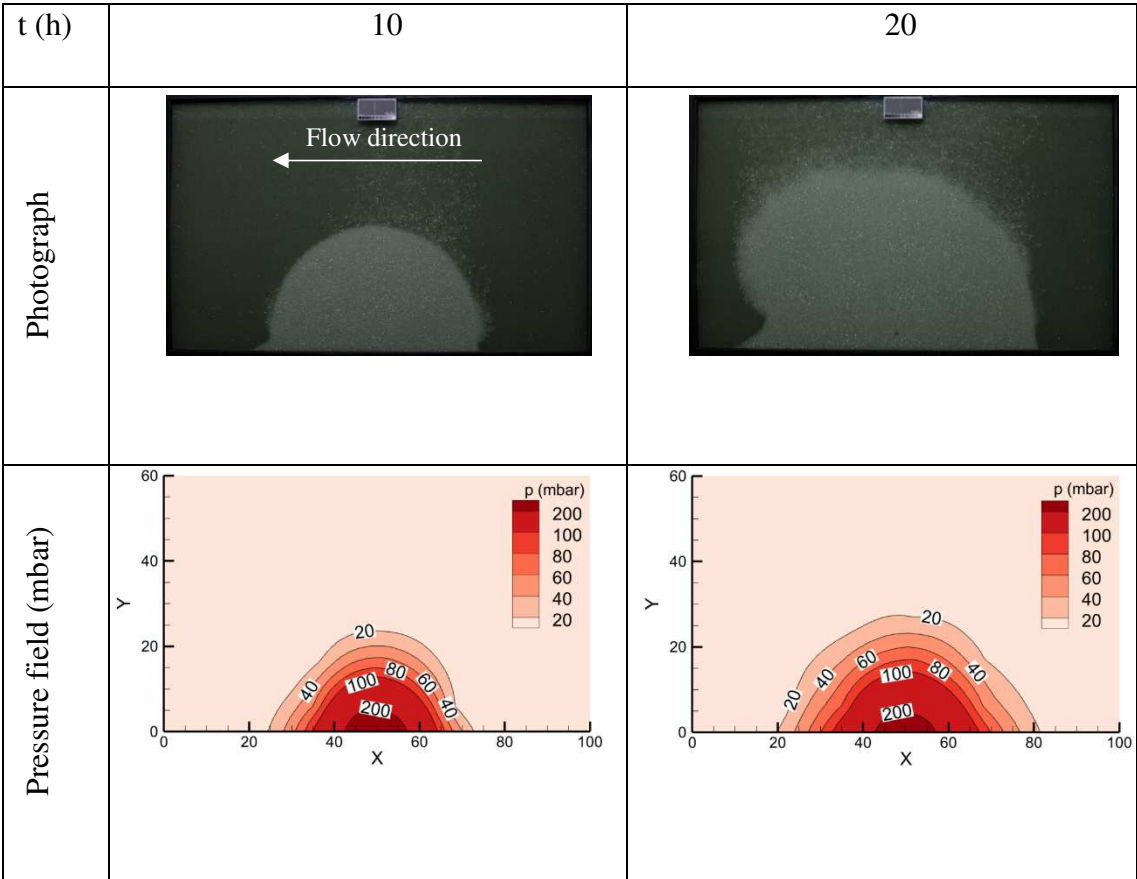
Once the foam reaches and fills the measurement radius of a probe, the saturation value decreases until it reaches a value close to 0. Since measurement precision is 0.1, we conclude that the liquid saturation after passing the foam is between 0 and 0.1. These values are in good agreement with the measurements carried out in columns [Aranda et al., 2020] where the liquid saturation ranged between 0.03 and 0.1 after a steady-state foam flow was reached.

These values also show the shape of the foam propagation quite well. The center TDR probe at (3,3) is the first to measure a decrease in saturation and to reach the final value of liquid saturation. Then the saturation falls, respectively, in sensors (3,2), (3,4) then (3,1). Probe (3,5) is hardly affected by the foam flow. This is coherent with the spherical shape of the foam propagation with an asymmetric extension on the left side due to the lateral flow which has been already observed by photographs and by calculating the aspect ratio (see [Davarzani et al., 2021]).

The rapid and smooth decrease in the saturation on the (3,3) probe shows that the foam flows as a strong foam, with a defined front. The (3,1) sensor shows behavior more like a mixture of weak foam and gas. The decrease in saturation is slower and marked by sudden

variations. This is due to the arrival of a train of gas bubbles in the area of the probe which abruptly reduces the liquid saturation. Since the weak foam front propagates more diffusely than the strong foam, the decrease observed is slow. However, the saturation decreases until it reaches a value close to those measured for the strong foam. The displacement of water by the weak foam is therefore comparable to that achieved by the strong foam in a slower regime.

We show in Figure 5 the saturation and pressure fields in the 2D tank after  $t = 10$  h, 20 h, and 29 h of injection using data from the 25 probes. Pressure fields are calculated by subtracting the hydrostatic pressure so that only the pressure variations due to foam injection and lateral flow are shown. Spatial interpolation between probes was performed using the kriging method [Davis and Sampson, 1986] implemented in Tecplot, a commercial software package. These fields are compared to the photographs in the background.



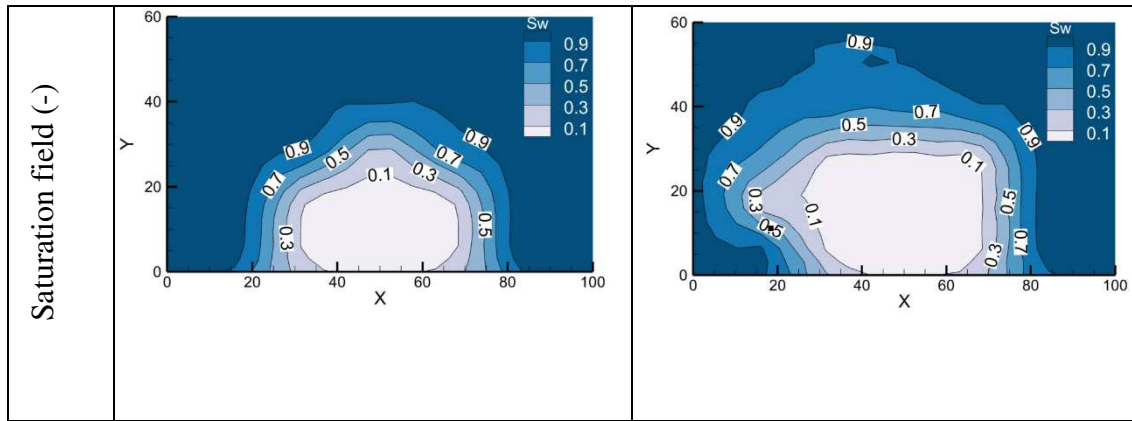


Figure 5 Photographs, pressure, and liquid saturation fields for different times (10 h and 20 h). The pressure and saturation fields are obtained from the interpolation of the measured data using Tecplot software (Kriging method). All axes are in cm. Lateral flow 1.4 m/day, foam quality 85%, and the total injection flow rate 8 mL/min.

Consistent with what has been observed with the injection pressures presented above, the pressure field inside the 2D tank also remains stable even if the front propagation continues to progress. Since the critical capillary pressure is reached at the injection point, which corresponds to the maximum pressure of the tank, the pressure field stabilizes in accordance with this value. These fields also show that the pressure generated by the lateral flow is negligible compared to the pressure generated by the foam flow. It can therefore be concluded that the pressure field will not change in the case of a prolonged injection. Weak foam will be generated in greater quantity to compensate for the increased radius by a loss of viscosity, and thus keep the pressure constant. Because of the distance between the pressure sensors and interpolation precision, it is not possible to capture the circular form of the foam using the pressure field.

Interpolating the data over the entire spatial domain does not accurately calculate the position of the front because of the distance between the sensors. The kriging interpolation method, therefore, creates a gradient between the two values.

Aside from the precise location of the front, the array of probes provides a correct picture of the reality of foam propagation. The saturation values in the strong foam are less than 0.1. Saturation is also very low in weak foam with values ranging between 0.1 and 0.3 which are particularly visible in this figure. Contrary to the pressure sensors, it is possible to capture the weak foam behavior using TDR sensors. Finally, the value of liquid saturation decreases very little in areas where the only upward flow of free gas occurs, above the zone of strong foam. The values are approximately 0.9 in these areas.

### 4.1.3. Comparison between TDR measurements and photographic analysis

In order to compare and validate the results obtained by the TDR probes and by the photographic analysis, the average liquid saturation values on a 5 cm square mesh (centered on the position of each TDR probe) were calculated by imaging. The parameters for the linear relation between optical density and water saturation after image calibration were  $\alpha = -1.54$ ,  $\beta = 2.98$  and  $I_{ref} = 19$ .

Figure 6 shows these results for row 3 of the 2D tank. The saturations calculated from the TDR probes are shown in solid lines and the saturations calculated from the photographic analysis are shown in dotted lines with marks. The saturation dynamics were the same with both methods. However, the values calculated by imaging are slightly shifted in time compared to those measured by TDRs. This could be explained by greater sensitivity in the imaging to the movements of free gas that precedes the arrival of the foam front or to a possible 3D edge effect, by which the gas bubbles would first move towards the 2D tank front glass. In this way, the gas would be fully captured by the photographic analysis while the TDR probe would only capture a little gas in its area of influence. Also, the under-prediction is more severe for probes (3,3) and (3,4). From the observation, we believe that there is more free gas in the center and right side of the tank compared to the left side because of the flow direction. These results, therefore, show the limits of these measurement methods, which are very useful for monitoring saturation variations, and relating them to the physical phenomena involved.

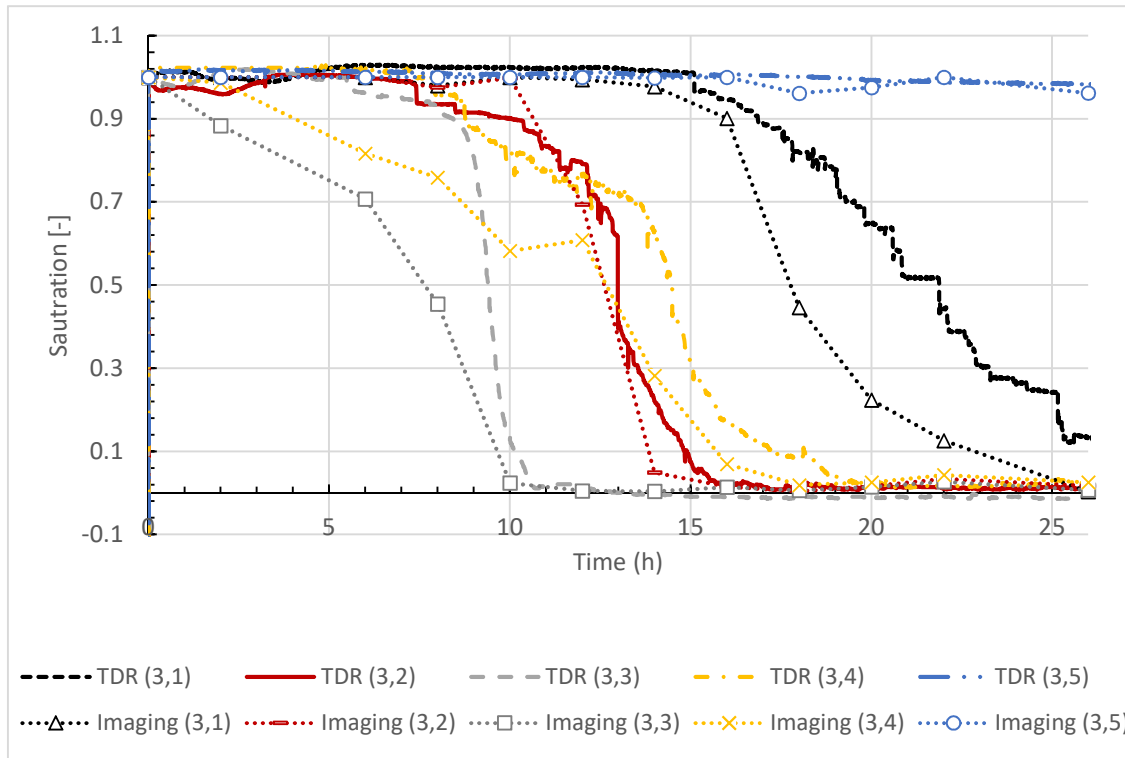


Figure 6 Water saturation as a function of time estimated by TDR probe measurements (solid lines) and by photographic analysis (dotted lines).

In Figure 7 we present 2D saturation fields, obtained by photographic analysis and TDR probes respectively. The same colors are used to represent the same ranges of saturation. As noted previously, the saturation fields obtained using TDR probes do not allow very precise visualization of the foam front because of the limited quantity of sensors. Photographic analysis can identify areas of strong and weak foam and the transitions between these areas. The advantage of TDR sensors is that they can be used in field monitoring. This comparison highlights the fact that the liquid saturation is slightly lower on the bottom part of the tank, around the injection point. This observation is valid for both methods and shows the presence of the drainage phenomenon at these time and space scales. The liquid phase flows down to the tank by gravity, resulting in a foam that is wetter than the center of the tank.

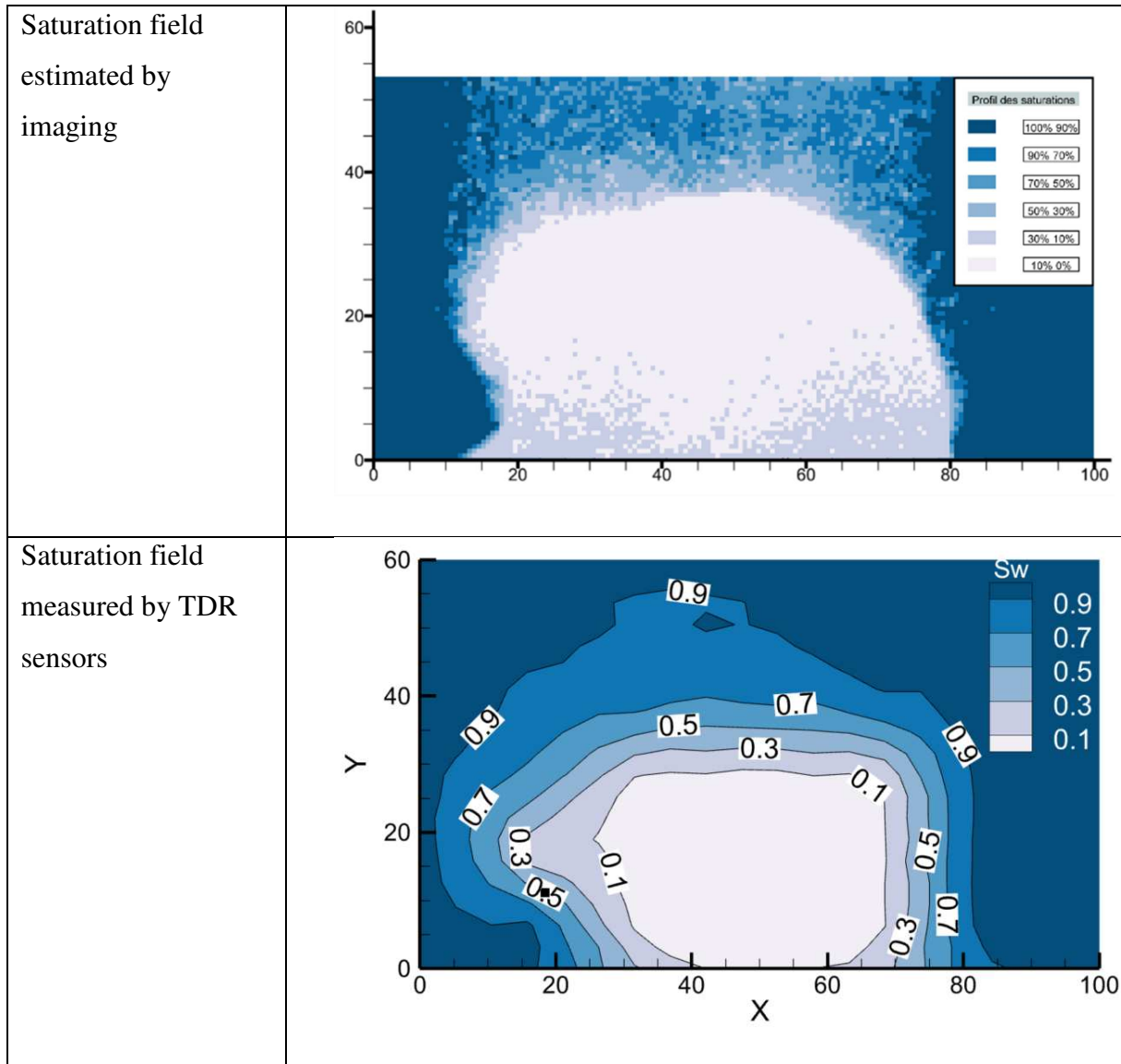


Figure 7 Comparisons of the liquid saturation fields calculated by analysis of TDR probes and estimated by imaging at  $t = 20$  h. The axes are in cm. Weak foam and trapped bubbles can be captured using imaging. The precision of the saturation obtained from TDR is sufficient to capture gas saturation (lateral flow 1.4 m/day, foam quality 85%, and the total injection flow rate 8 mL/min).

## 4.2. Model parameters, numerical simulation, and results

### 4.2.1. Two-phase flow hypothesis and estimation of parameters

It has been observed experimentally that viscous effects are dominant over capillary effects during foam flow in highly permeable porous media [Aranda et al., 2020]. During strong foam (fine-textured foam) flow in highly permeable porous media, the foam displacement is quite stable and seems to be piston-like [Aranda et al., 2020]. This means that  $\frac{\partial p_c}{\partial S_w}$  in equation (11) tends towards zero. In the van Genuchten-Mualem model for the relative permeabilities (equations 16 and 17),  $m$  tends towards 1. [Chen et al., 1999; Mualem, 1976] However, we

considered a constant and small value for the capillary diffusion coefficient  $D_c = 2 \times 10^{-5} \text{ Pa} \cdot \text{s}$  (see equation 10) to improve the model convergence.

The calculated parameters necessary to solve the above equations numerically are listed in Table 2. The wetting phase viscosity and density are those of water at 20 °C. The non-wetting phase is the foam. Foam is injected at a quality of 85%. The estimated density using this gas volume fraction is  $150 \text{ kg} \cdot \text{m}^{-3}$ . As seen previously, its viscosity is that of gas multiplied by a mobility reduction factor (MRF). The permeability and porosity of the medium were measured in the laboratory.

*Table 2. Main parameters of the two-phase flow model in the 2D tank.*

Parameters	Values
$\rho_w$	$1 \times 10^3 \text{ kg} \cdot \text{m}^{-3}$
$\rho_{nw}$	$1.5 \times 10^2 \text{ kg} \cdot \text{m}^{-3}$
$\mu_w$	$1 \times 10^{-3} \text{ Pa} \cdot \text{s}$
$\mu_{nw}$	$MRF \times 1.8 \times 10^{-5} \text{ Pa} \cdot \text{s}$
$K_{int}$	$8.4 \times 10^{-10} \text{ m}^2$
$\phi$	0.37

The lateral injection velocity corresponds to the apparent velocity in the 2D tank set at 1.4 m/day multiplied by the porosity (Darcy velocity). In this model, the lateral flow is reversed to match the experimental data obtained from the back of the 2D tank (flow from right to left).

From the parameters presented in Table 2, the viscosity of the invading fluid (foam) is much higher than the displaced fluid (water). However, the invading fluid density is lower than the displaced fluid. According to the stability of the two-phase flow criterion [Glass and Nicholl, 1996], the intrusion of foam more viscous than water into a water-saturated soil is conditionally stable for an upward flow. The critical velocity of the fluid front propagation stability between foam and water interface can be written as [Glass and Nicholl, 1996]

$$U_c = \frac{|\rho_{nw} - \rho_w| g K_{int}}{\phi |\mu_{nw} - \mu_w|} \quad (32)$$

From this equation, we obtain  $U_c = 2.4 \times 10^{-6}$  m/s, which is less than foam injection velocity  $U_{inj} = 7.8 \times 10^{-5}$  m/s. Therefore, the foam/water interface should be stable.

To stabilize the calculation in equation (10), the capillary diffusion  $D_c$  was set at  $2 \times 10^{-5}$  Pa·s. This capillary diffusion creates a capillary fringe at the foam/water interface. The value chosen is the lowest value leading to stabilization of the model for the optimal mesh.

According to the experimental results (see also [Davarzani et al., 2021]), three main phenomena have an impact on the viscosity of the foam in highly permeable porous media: the non-Newtonian behavior, the critical capillary pressure, and the surfactant concentration. The objective is therefore to incorporate these three phenomena into the MRF model.

- **Non-Newtonian behavior**

The non-Newtonian behavior is modeled from the power-law measured in [Aranda et al., 2020], obtained for the same foam and porous media, as below

$$\mu_{app} = 5.7 \dot{\gamma}^{-0.56} \quad (3)$$

where  $\mu_{app}$  is the foam apparent viscosity (Pa·s) and  $\dot{\gamma}$  the shear rate ( $s^{-1}$ ). Given that the primary variables are mixed pressure and saturation, we introduce the non-Newtonian behavior in terms of the pressure gradient, using the experimental data (see Appendix B)

$$\mu_{app} = 278 \nabla p^{-0.39} \quad (3)$$

where  $\nabla p$  is the pressure gradient ( $Pa \cdot m^{-1}$ ) generated during the flow of foam in the column experiment [Aranda et al., 2020].

This law can be reformulated by expressing the apparent viscosity as a function of a reference case and the gas viscosity,

$$\mu_{app} = \mu_g MRF_{ref} \left( \frac{\nabla p}{\nabla p_{ref}} \right)^{n_p - 1} \approx \mu_g \left( 1 + MRF_{ref} \left( \frac{\nabla p}{\nabla p_{ref}} \right)^{n_p - 1} \right) \quad (3)$$

5)

where  $\mu_g$  is the viscosity of the gas (Pa·s),  $MRF_{ref}$  the reference mobility reduction coefficient (-) at the pressure gradient  $\nabla p_{ref}$  (Pa·m<sup>-1</sup>), and  $n_p$  the exponent of the power-law associated with the pressure gradient (-), equal to 0.61. The equality is valid because with the high foam viscosity,  $MRF_{ref} \left( \frac{\nabla p}{\nabla p_{ref}} \right)^{n_p-1}$  is of the order of 105  $\gg$  1.

Finally, a minimum pressure gradient  $\nabla p_{min}$  is introduced to prevent the viscosity from tending to infinity for low-pressure gradients. Thus, if  $\nabla p < \nabla p_{min}$ , the viscosity becomes constant with regard to the non-Newtonian behavior such as

$$\mu_{app} = \mu_g \left( 1 + MRF_{ref} \left( \frac{\nabla p_{min}}{\nabla p_{ref}} \right)^{n_p-1} \right) \quad (3)$$

(6)

- **Impact of surfactant concentration**

The impact of the surfactant concentration could not be directly measured experimentally. We estimated its effect based on the results obtained by [Wang et al., 2012]. The apparent viscosity is equal to that of the gas without the presence of surfactant and increases with concentration until its stabilization around the critical micelle concentration (CMC) [Wang et al., 2012]. The smoothed Heaviside function related to the surfactant concentration  $f_c$ , plotted in Figure 8, represents the influence of the surfactant concentration. It is firstly composed of a ramp going from point (0, 0) to point (CMC, 1) then a stabilization at 1 after the CMC. The function is numerically smoothed to be differentiable twice at any point.

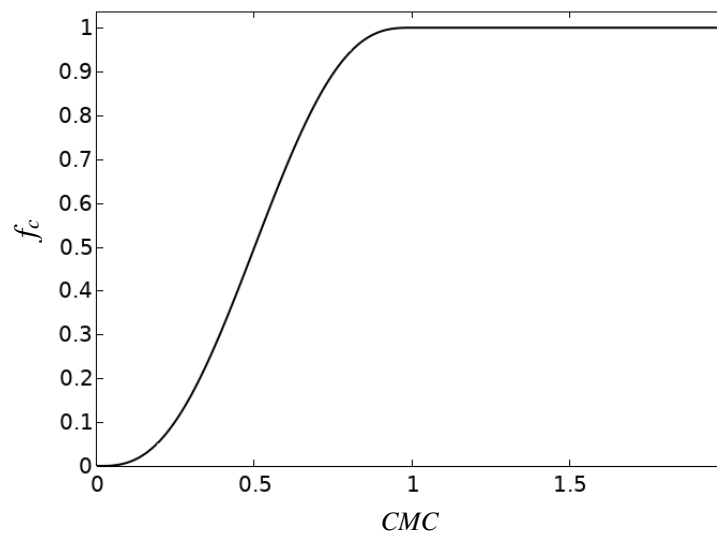


Figure 8.  $f_c$  as a function of concentration, normalized with the CMC (critical micelle concentration).

- **Impact of the critical capillary pressure**

The apparent viscosity drops when the capillary pressure exceeds the critical capillary pressure as the foam coalesces and becomes coarser. As observed before, this phenomenon can be responsible for stabilizing the injection pressure. To represent this, a smoothed Heaviside function  $f_p$  is introduced which is equal to 1 up to the critical capillary pressure, fixed at the experimentally measured value of 195 mbar, then 0 after this. For the needs of numerical stability, this curve is numerically smoothed on a transition zone of  $p_c^*/5$  and is differentiable twice at any point.

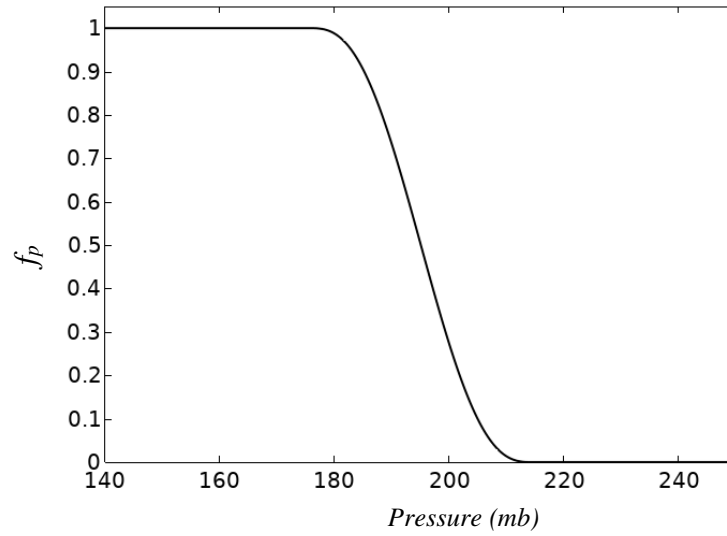


Figure 9.  $f_p$  as a function of pressure.

- **Final MRF coefficient**

The complete MRF incorporating these three phenomena therefore takes the following form

if  $\nabla p \geq \nabla p_{min}$ :

$$MRF = 1 + MRF_{ref} \left( \frac{\nabla p}{\nabla p_{ref}} \right)^{n_p-1} f_c(c) f_p(p) \quad (3)$$

if  $\nabla p < \nabla p_{min}$ :

$$MRF = 1 + MRF_{ref} \left( \frac{\nabla p_{min}}{\nabla p_{ref}} \right)^{n_p-1} f_c(c) f_p(p) \quad (8)$$

where  $MRF_{ref}$  is the reference mobility reduction factor (-) to the reference pressure gradient  $\nabla p_{ref}$  ( $\text{Pa} \cdot \text{m}^{-1}$ ),  $\nabla p$  is the pressure gradient ( $\text{Pa} \cdot \text{m}^{-1}$ ),  $\nabla p_{min}$  the minimum pressure gradient to

observe the non-Newtonian behavior ( $\text{Pa}\cdot\text{m}^{-1}$ ),  $n_p$  the exponent of the power-law associated with the pressure gradient (-),  $f_c$  and  $f_p$  two smoothed Heaviside functions varying between 0 and 1,  $c$  the surfactant concentration ( $\text{mol}\cdot\text{m}^{-3}$ ), and  $p$  the pressure (Pa).

The reference pressure gradient was first chosen equal to  $1.7\times 10^5 \text{ Pa}\cdot\text{m}^{-1}$ , which corresponds to a  $MRF_{ref}$  of  $1.5\times 10^5$  obtained experimentally using a 1D column (see [Aranda et al., 2020]). However, this value was found to be insufficient to match the modeled injection pressure to the experimentally measured one. It was necessary to adjust this parameter to match the measured injection pressure. The adjusted  $MRF_{ref}$  value was  $4.4\times 10^5$ . This difference can have multiple sources, such as the 2D flow hypothesis. However,  $MRF_{ref}$  is always of the order of magnitude of  $10^5$ . The minimum pressure gradient has been set at  $1\times 10^4 \text{ Pa}\cdot\text{m}^{-1}$ , which corresponds to a maximum apparent viscosity of the foam of  $24.2 \text{ Pa}\cdot\text{s}$ . Table 1 lists all the parameters used to set up this model.

*Table 1 List of parameters needed for modeling*

Parameter	Definition	Value
$L$	2D tank length	1 m
$h$	Height of saturated porous media	0.6 m
$d$	Injection point diameter	0.02 m
$e$	2D tank internal width	0.085 m
$Q_{inj}$	Foam injection flow rate	$8 \text{ ml}\cdot\text{min}^{-1} = 1.3\times 10^{-7} \text{ m}^3\cdot\text{s}^{-1}$
$U_{inj}$ $= Q_{inj}/(d \times e)$	Foam injection velocity	$7.8\times 10^{-5} \text{ m}\cdot\text{s}^{-1}$
$U_{lat} = U_{lat,app} \times \phi$	Lateral flow velocity	$6.0\times 10^{-6} \text{ m}\cdot\text{s}^{-1}$
$D_c$	Capillary diffusion coefficient	$2\times 10^{-5} \text{ Pa}\cdot\text{s}$
$MRF_{ref}$	Adjusted reference mobility reduction factor	$4.4\times 10^5$
$n_p$	Power law exponent for non-Newtonian relationship	0.61
$\nabla p_{ref}$	Reference pressure gradient	$1.7\times 10^5 \text{ Pa}\cdot\text{m}^{-1}$
$\nabla p_{min}$	Minimum pressure gradient	$1\times 10^4 \text{ Pa}\cdot\text{m}^{-1}$

#### 4.2.2. Numerical simulation, boundary, and initial conditions

The objective was to model only the behavior of the strong foam. The free gas rise and weak foam were not modeled. The chosen mesh, refined in terms of foam injection and the outlet of the flows, makes it possible to obtain a stable model.

We used COMSOL<sup>®</sup> Multiphysics to solve two-phase flow in porous media based on the mixture model. However, the Two-Phase Darcy's Law module of COMSOL does not use the same equations as Wang and Beckermann's (1993) formulation. Therefore, we modified these equations to be fully matched to the chosen formulation (see Appendix A). We used second-order elements for the velocity components and linear elements for the pressure field (P2+P1) to discretize the two-phase Darcy's law equation. Linear elements were used for the concentration to discretize the diffusion-advection equation. The simulation domains were discretized by triangular meshes with 7,848 elements under the constraint of maximum and minimum element sizes of 0.01 m and  $2.25 \times 10^{-5}$  m, respectively. The mesh is refined at the foam injection boundary and the right border of the domain to a maximum element size of 0.005 m to enhance the model convergence and avoid numerical artifacts. The maximum element growth rate was 1.05.

We used the Backward Differentiation Formula (BDF) time-stepping method with the "Free" time stepping option. Free time-stepping allows the solver to take larger or smaller time-steps as required to satisfy the specified tolerances. The solvers will try to take as large a time-step as possible but will reduce the time-step size when necessary if the solution starts to vary rapidly in time.

The selected boundary conditions that fulfill the experimental setup conditions for two-phase flow are presented in Figure 10.

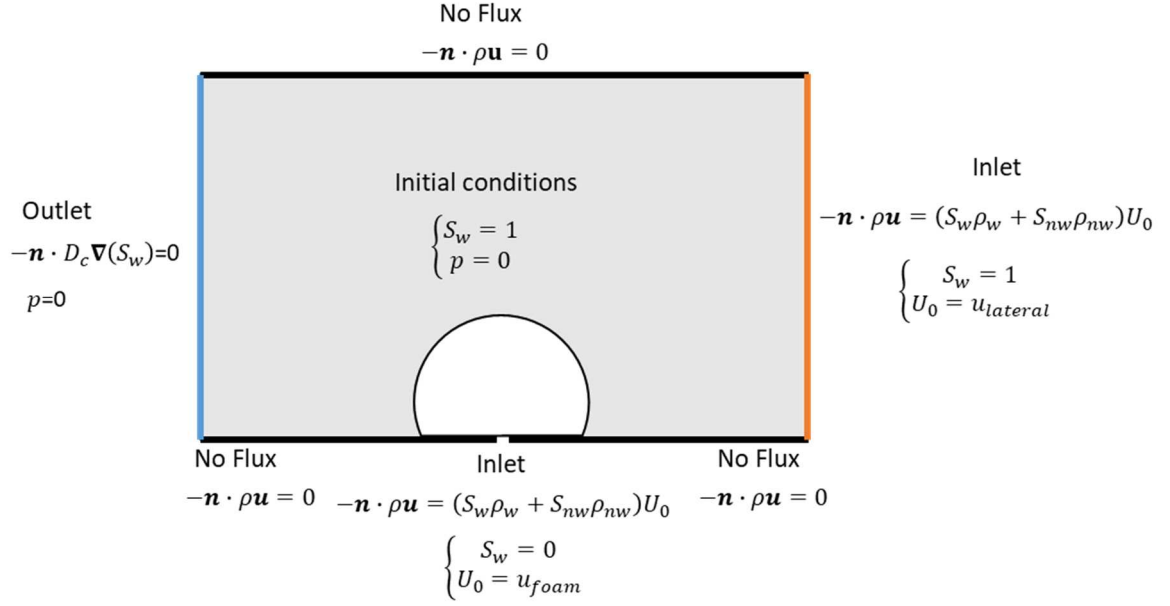


Figure 10 Boundary and initial conditions for two-phase flow equations (the vector  $\mathbf{n}$  is the unit normal vector).

On the lower (excluding injection segment) and upper borders of the geometry, we consider that the normal flow velocity is zero in the direction normal to the border. The experimental results presented before indeed show that the interface between the unsaturated porous medium and the saturated porous medium is not modified during the experiment. Therefore, there is no normal flow at this interface.

$$-\mathbf{n} \cdot \rho \mathbf{u} = 0 \quad (3)$$

For the left border and the foam injection segment, the boundary conditions correspond to a fluid inlet. The value of the saturation is imposed as well as that of the pressure, indirectly by a velocity. This inlet boundary condition reads

$$-\mathbf{n} \cdot \rho \mathbf{u} = (S_w \rho_w + S_{nw} \rho_{nw}) U_0 \quad (4)$$

where  $U_0$  is the total injection velocity of the two phases ( $\text{m} \cdot \text{s}^{-1}$ ). The values of  $S_w$  and  $U_0$  are defined according to the considered border.

Finally, the right boundary condition corresponds to the outlet boundary condition of the fluids according to experiments in the 2D tank. The pressure is, therefore, imposed to

atmospheric pressure and the contribution of capillary diffusion in the direction normal to the wall is zero.

$$-\mathbf{n} \cdot D_c \nabla S_w = 0 \quad (4)$$

$$p = p_{atm} \quad (1)$$

where  $p_{atm}$  (Pa) is the atmospheric pressure.

The initial saturation and pressure conditions correspond to the tank completely saturated with water and to a zero-pressure field in the absence of flow and neglecting gravity.

$$\begin{cases} S_w(t = 0) = 1 \\ p(t = 0) = p_{atm} \end{cases} \quad (4) \quad (2)$$

Solute transport is governed by the differential advection-diffusion equation in porous media. The selected boundary conditions according to the experimental conditions are presented in Figure 11. On the lower (except the injection segment) and upper borders, there is no flow in the normal direction. There is also no diffusion in this direction. A no-Flux boundary condition was imposed in these boundaries as

$$\mathbf{n} \cdot (\mathbf{D}_{eff} \cdot \nabla c) = 0 \quad (4) \quad (3)$$

On the injection segment boundary, a surfactant concentration was provided by the foam injection. A constant flow of concentration on this boundary is therefore imposed. This is an Inflow boundary condition

$$\mathbf{n} \cdot (-\mathbf{D}_{eff} \cdot \nabla c + \mathbf{u}c) = \mathbf{n} \cdot (\mathbf{u}c_{in}) \quad (4) \quad (4)$$

On the left border, the flow of pure water does not provide surfactant. The limiting conditions are thus the same as previously but in the form of

$$\mathbf{n} \cdot (-\mathbf{D}_{eff} \cdot \nabla c + \mathbf{u}c) = 0 \quad (4) \quad (5)$$

On the right border, the surfactant can freely flow out of the domain. This is a convective boundary condition or Outflow.

$$\mathbf{n} \cdot (\mathbf{D}_{eff} \cdot \nabla c) = 0 \tag{4}$$

$$\tag{6}$$

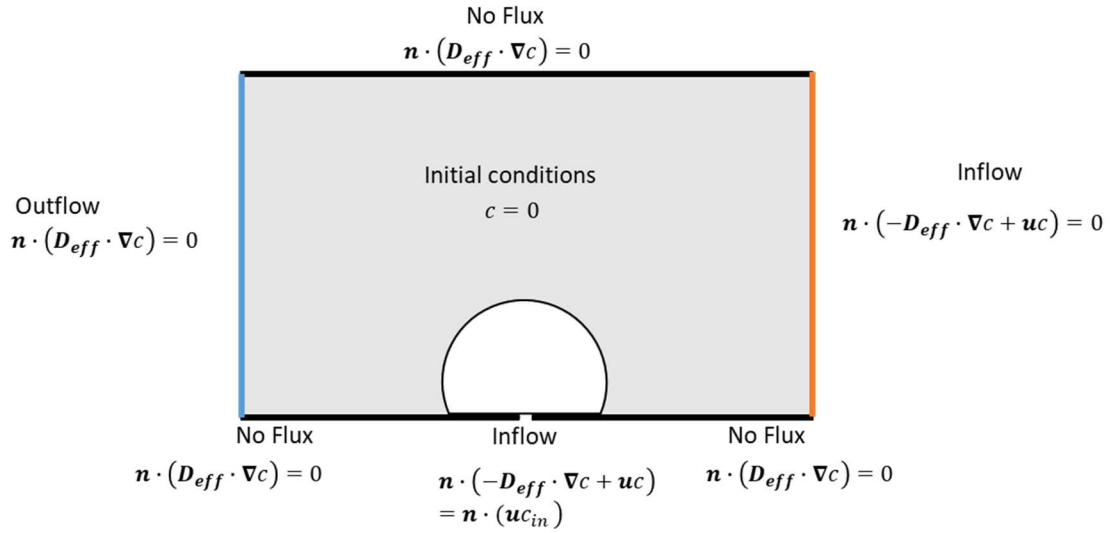


Figure 11 Boundary and initial conditions for solute transport equations.

#### 4.2.3. Comparison with experimental results

We compared the results obtained by numerical simulation (saturation and pressure fields) with the results obtained experimentally. As the modeling concerns only the flow of the strong foam, only the experimental results concerning this situation were analyzed.

##### - *Foam propagation shape and blocking effect*

Figure 12 shows the foam saturation field as well as the flow streamlines at  $t = 10$  h and  $t = 20$  h, respectively. The capillary diffusion fringe is visible but our interest is focused on the shape of the strong foam, represented by a foam saturation equal to 1 (foam quality of 85%). Following the results observed experimentally, the foam forms a half-disk centered on the injection point. The streamlines show that the lateral flow is indeed diverted by the foam flow, as shown by the experimental tracing tests [Davarzani et al., 2021]. These results show that the implemented equations correctly model the shape of the foam and its ability to divert water flows.

t (h)	Model results	Experimental results
----------	---------------	----------------------

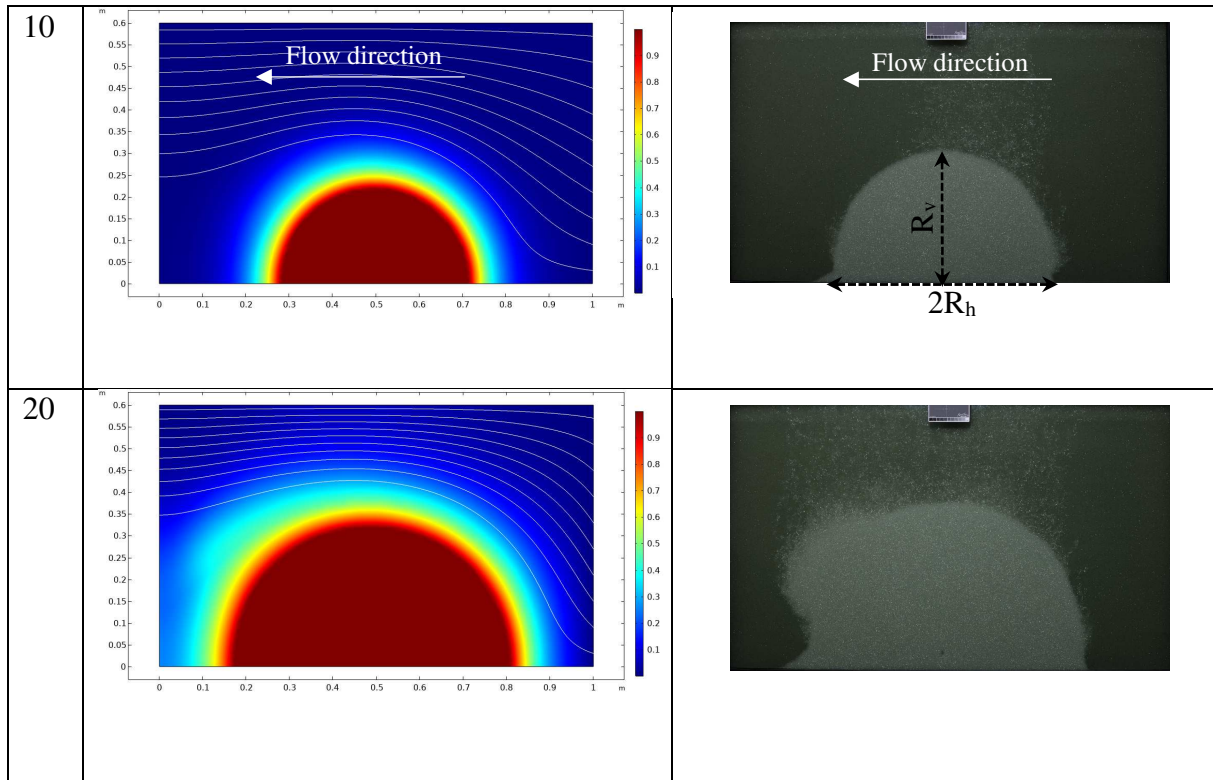


Figure 12 Simulated streamlines and saturation fields at  $t = 10$  h and 20 h. Comparison with experimental data (photographs). The streamlines show that the lateral flow is indeed diverted by the flow of the foam. The proposed model can simulate the shape of the foam and its ability to divert groundwater flows.

Figure 13 compares the change of the radius of influence (ROI) obtained numerically with the radius of influence measured during the experiment. The radius of influence of the foam can be defined as the geometric mean of the lateral radius  $R_h$  and the vertical radius  $R_v$  as  $ROI = \sqrt{R_h R_v}$ . The radius of influence obtained by modeling corresponds to the radius at which the foam saturation becomes less than 1 (start of the capillary fringe).

At the beginning of the injection, the numerically calculated radius of influence is slightly less than that obtained experimentally. This is due to the loss of mass through the numerical capillary fringe. It has been observed experimentally that there is very little coalescence at the start of the injection and therefore almost all of the injected mass flows in the form of a strong foam. In numerical modeling, part of the mass diffuses into the capillary fringe because of the non-zero capillary diffusion coefficient. For this same reason, the numerically calculated radius of influence becomes larger than that measured experimentally at the end of the injection, where the coalescence becomes greater while the numerical capillary diffusion remains constant. The slight delay before increasing the radius of influence is due to non-Newtonian behavior. In the first moments, the pressure gradient is very high at the level of the

injection segment and as a result, the viscosity is greatly reduced. We did not observe this phenomenon experimentally.

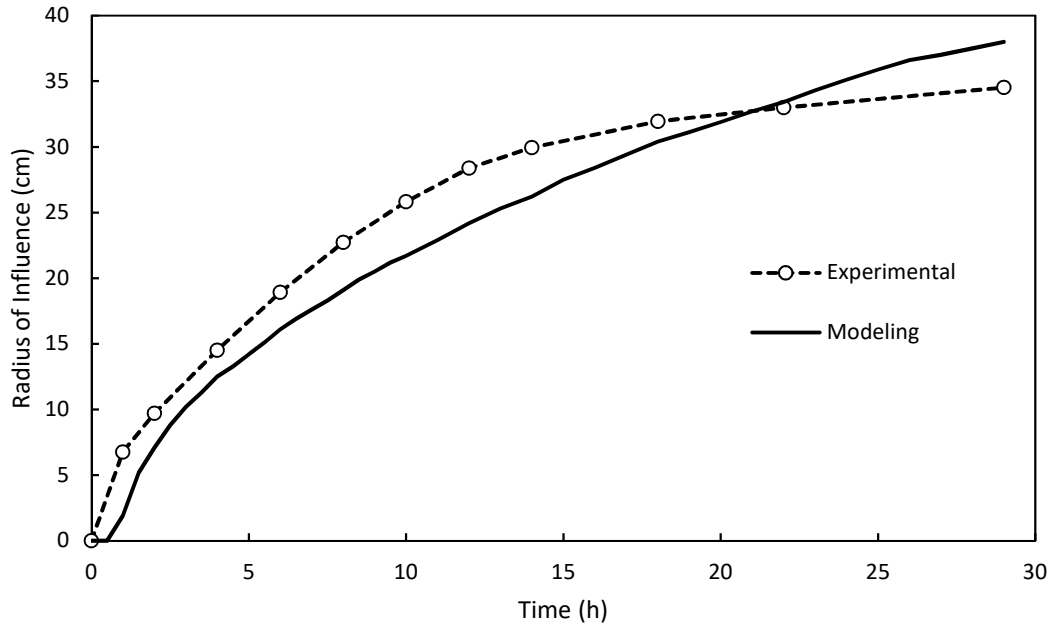


Figure 13 Comparison of the radius of influence of foam propagation between numerical and experimental results. The model can predict the foam propagation front with a precision error of less than 5%.

The experimental and numerical fields for ROI are quite similar, which supports the two-dimensional approach hypothesis. The maximum measured error is 15%. These results also show the limits of such a model where the coalescence at the foam/water interface during the injection phase is not modeled.

#### - *Pressure fields*

Figure 14 compares the injection pressure obtained from the numerical model with the experimental measurements. The decrease in viscosity when the critical pressure is reached (function  $f_p$ ) in the MRF gives a numeric injection pressure which stabilizes quickly. The pressure measured experimentally is subject to further variation. This can be explained by complex foam flow behavior in porous media compared to a simplified empiric model e.g., the compressibility [Omirbekov et al., 2020b], avalanches of coalescence events [Höhler and Cohen-Addad, 2005], or preferential foam flow paths. The precise simulation of the foam behavior needs the mechanistic approach (e.g., bubble population balance models) to accurately assess bubble formation, destruction, and propagation. Although our model cannot precisely predict the pressure behavior, it does allow us to predict the general behavior of

foam flow in porous media (e.g., pressure stabilization). From this result, we calibrate the  $R_{ref}$  parameter so that the critical injection pressure is reached almost simultaneously experimentally and by modeling. The slight delay at the start of the injection for model results is due to the non-Newtonian behavior, as stated previously.

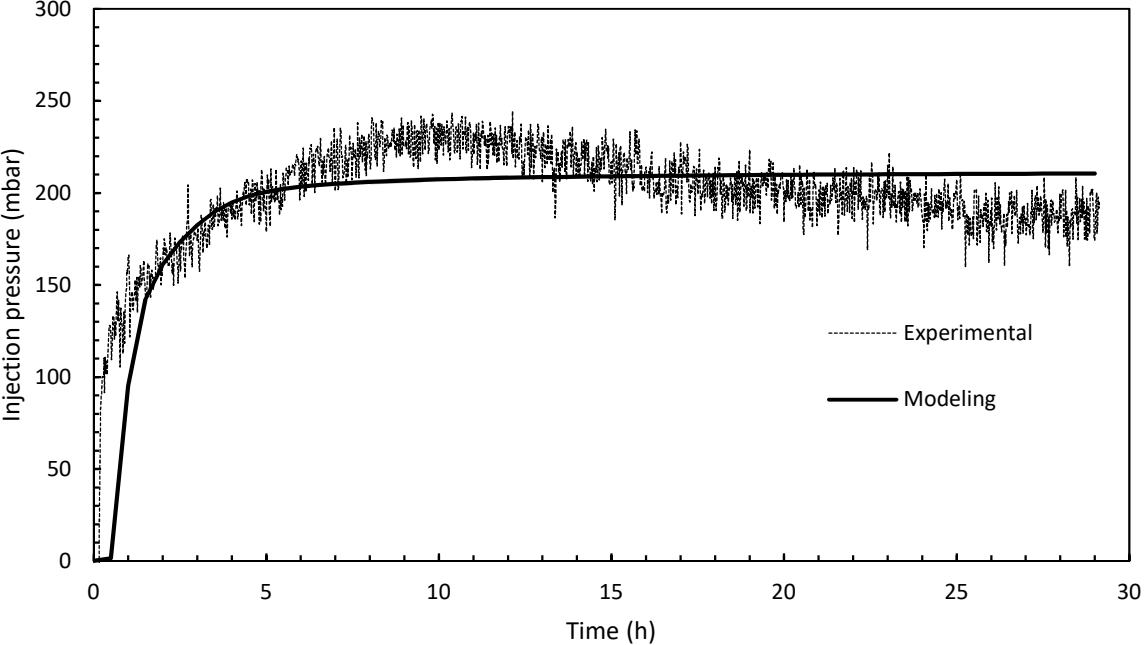


Figure 14 Comparison between the numerical and experimental changes in injection pressure over time. The proposed model predicts the experimental pressure variations well. A logarithmic increase in pressure followed by stabilization of the pressure was observed. The pressure stabilization state can be explained by a state of pseudo-equilibrium between foam generation and destruction.

Figure 15 represents the pressure fields from modeling and the measurements by pressure sensors in the 2D tank. The pressure fields from the experiment are established from 26 point measurements and, therefore, the data are interpolated or extrapolated to get the pressure field. Hydrostatic pressure has been calculated and subtracted from all measurements.

t (h)	Model results	Experimental results
----------	---------------	----------------------

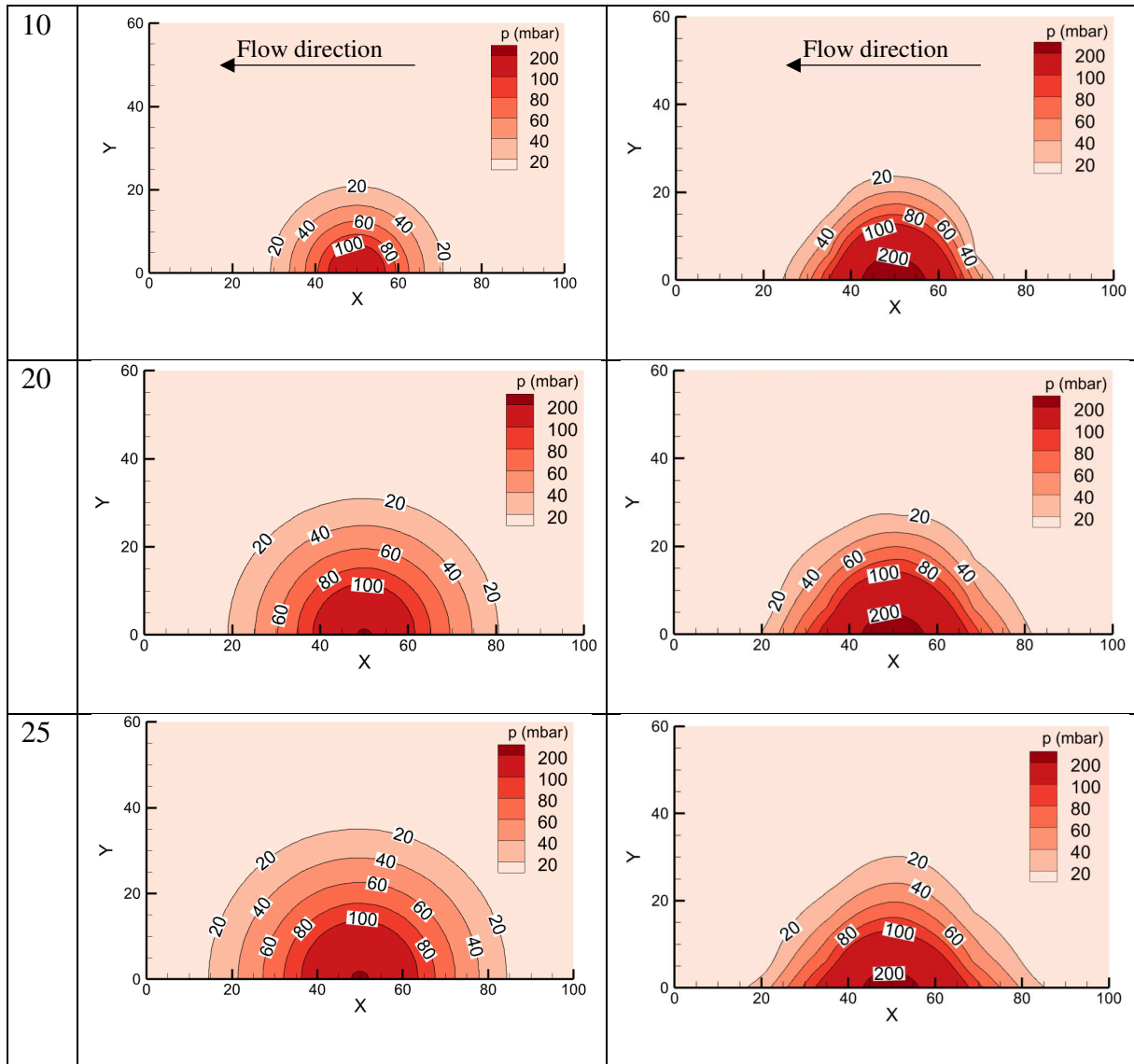


Figure 15 Comparison between the numerical and experimental changes in the pressure field over time. Hydrostatic pressure has been calculated and subtracted from all measurements. The experimental pressure fields are obtained from the interpolation of the measured data using Tecplot commercial software (Kriging method).

We notice that the pressure fields obtained from modeling have a more progressive change over time while the experimental fields hardly show changes after  $t = 20$  h. The experimental results show a higher gradient (contours are more closely packed) away from the injection point compared to the model results. This can be because of the compressibility effect in a transient regime and the interpolation precision. Modeling shows that the high-pressure zone is very localized at the injection point. This area is probably overestimated by the interpolation of the experimental measurements. The modeling shows a slight asymmetry in the pressure field from the 2D tank central axis because of the water lateral flow. This is partially confirmed by the experimental data. The lack of data in the bottom 2D tank

boundary may explain the deviation of the experimental pressure field from the half-disk form.

## 5. Conclusions

We studied how foam flows in highly permeable porous media numerically and experimentally in a meter-scale 2D tank. The pre-generated foam was injected through the center bottom of the 2D tank. Foam propagation was monitored using the light-reflected method, thanks to the tank's transparent front glass, and pressure and time-domain reflectometer (TDR) sensors installed in the rear of the tank. The experiments allowed us to study the behavior of the foam flowing in a highly permeable porous medium made of 1 mm glass beads under lateral water flow.

During the foam injection, the pressure increased according to a logarithmic law which is the usual behavior of the pressure profile for radial fluid flow [Wu and Pruess, 2000]. Even if the injection continued, the pressure increase diminished and became a quasi-plateau. This phenomenon can be related to foam coalescence close to the foam propagation front and increasing the local capillary pressure to its critical value near the injection point. The fact that the pressure generated by foam can be stabilized during the injection is of great interest for foam injection at the field scale.

The saturation profile obtained from imaging and TDR sensors showed that the foam propagation was spherical with an asymmetric extension on the left side due to the lateral flow. TDR sensors were able to predict the shape of the foam propagation with good precision including strong and weak foam zones. The saturation field obtained using the imaging technique identified areas of strong and weak foam zones and also the border of foam propagation. However, the main advantage of using TDR probes is that they can be used in real cases of field monitoring. Interpolating the pressure data over the entire 2D tank surface did not produce the correct image of the foam-flow propagation shape. This low prediction precision is mainly because of the precision of the pressure sensors that does not allow for the detection of the weak foam zones. These results will allow the selection of a suitable method for monitoring foam flow in highly permeable porous media in future laboratory-scale experiments and field-scale tests.

Our model incorporates the main parameters influencing foam flow behavior in highly permeable porous media through a reduction in gas-phase mobility. Non-Newtonian behavior was introduced as a power-law relationship obtained experimentally. The concentration of

surfactant and critical pressure also play an important role in foam coalescence, and consequently, in how foam viscosity varies.

The numerical model can correctly capture the shape and propagation of strong foam, and its ability to divert water flows, which is already confirmed by the tracing tests. The mobility reduction factor we chose allowed us to capture the pressure variation behavior observed experimentally. The model predicts the pressure values measured experimentally well. The experimental results show a higher pressure gradient from the injection point with a more conical shape than the model results. The higher pressure gradient in experimental data may be because of the compressibility, which is not taken into account in the model. One other possible reason for this small discrepancy can be related to the interpolation precision. The difference between the shapes of the experimental and modeling pressure fields is due to the lack of pressure sensors on the bottom boundary of the 2D tank, and therefore, the low precision of the interpolation in this zone. Therefore, this model can be used to predict foam injection processes in highly permeable porous media such as for soil remediation applications.

### **Acknowledgments**

This study was performed as part of the “Famous” project. The authors would like to thank ADEME for co-funding the project under the “GESIPOL” program and BRGM/DEPA and Solvay France for providing the PhD grant for Romain Aranda. We gratefully acknowledge the financial support provided to the PIVOTS project by the “Région Centre – Val de Loire” and the European Regional Development Fund.

## Appendix. A Modifications applied to COMSOL Two-Phase Darcy's Law module

COMSOL offers a module for solving two-phase flow equations in porous media called “Two-Phase Darcy's Law”. This module is based on the skeleton of the “mixture model”, without taking gravity into account. However, this module does not use the same equations as Wang and Beckermann (1993). The differences between the COMSOL mixture model and Wang and Beckermann (1993) are presented in Table A.1.

Table A.1. Differences between COMSOL Two-phase Darcy's law and the mixture model proposed by Wang and Beckermann (1993)

COMSOL Two-Phase Darcy's Law	Wang and Beckermann (1993)
$\frac{1}{\mu} = S_w \frac{\kappa_{r,w}}{\mu_w} + S_{nw} \frac{\kappa_{r,nw}}{\mu_{nw}}$	$\mu = \frac{\rho}{\frac{\rho_w \kappa_{r,w}}{\mu_w} + \frac{\rho_{nw} \kappa_{r,nw}}{\mu_{nw}}}$
$\frac{\partial(\phi S_w \rho_w)}{\partial t} + \nabla \cdot (S_w \rho_w \mathbf{u})$ $= \nabla \cdot (D_c \nabla (S_w \rho_w))$	$\frac{\partial(\phi S_w \rho_w)}{\partial t} + \nabla \cdot [\lambda_w \rho \mathbf{u}]$ $= \nabla \cdot \left[ D_c \nabla S_w - \frac{\rho K_{int}}{\mu} \lambda_w \lambda_{nw} \Delta \rho \mathbf{g} \right]$
$D_c = -\frac{\kappa_{r,w}}{\mu_w} K_{int} (S_w - 1) \frac{\partial p_c}{\partial S_w}$	$D_c = -\frac{\rho K_{int}}{\mu} \lambda_w \lambda_{nw} \frac{\partial p_c}{\partial S_w}$

In this study, we used the exact mixture model proposed by [Wang and Beckermann, 1993]. The COMSOL equations were therefore modified using the Equation view tools.

## Appendix. B Apparent foam viscosity as a function of pressure gradients measured in column experiments

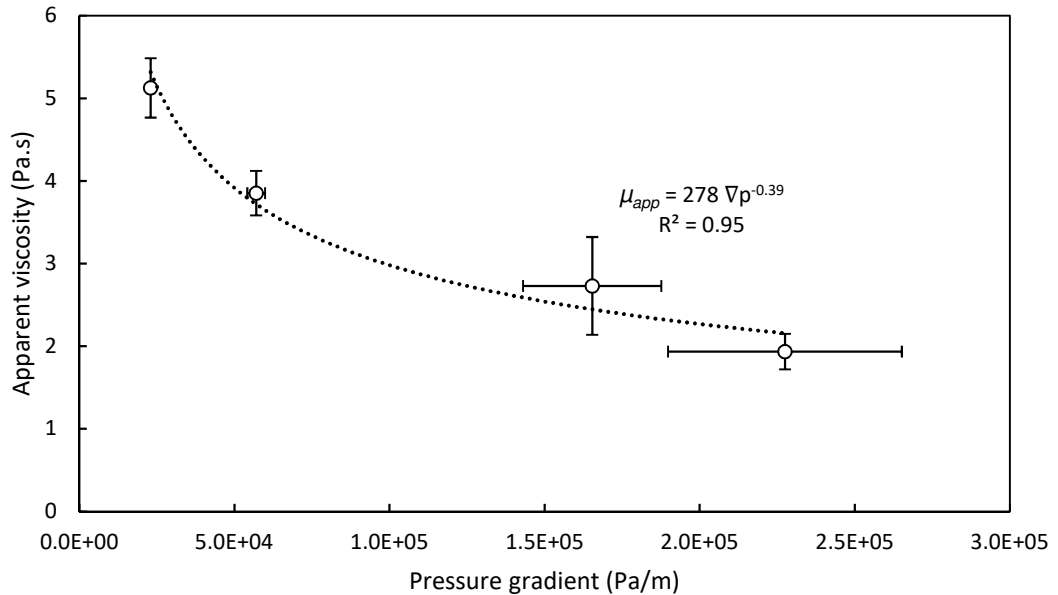


Figure B.1. Apparent viscosity as a function of pressure gradient that measured during the flow of foam in the column experiment [Aranda et al., 2020]. The markers indicate the original data points and the dashed line presents the fitted power-law function.

### References

[Almajid et al., 2021] Almajid, M. M., Wong, Z. Y. and Kovscek, A. R.: 2021, Mechanistic foam flow model with variable flowing foam fraction and its implementation using automatic differentiation, *Advances in Water Resources* **150**, 103877. <https://www.sciencedirect.com/science/article/pii/S0309170821000324>

[Aranda et al., 2020] Aranda, R., Davarzani, H., Colombano, S., Laurent, F. and Bertin, H.: 2020, Experimental study of foam flow in highly permeable porous media for soil remediation, *Transport in Porous Media* **134**(1), 231–247. <https://doi.org/10.1007/s11242-020-01443-8>

[Azmi et al., 2019] Azmi, N. S. M., Bakar, N. F. A., Abdullah, M. A. M., Latif, A. H. A. and Mohd, T. A. T.: 2019, 2D-silica ring interactions with alpha olefin sulphonate (AOS) surfactant under AOS/water system using molecular dynamic simulation, *Malaysian Journal of Chemical Engineering & Technology* **2**, 1–7.

[Bertin et al., 2017] Bertin, H., Del Campo Estrada, E. and Atteia, O.: 2017, Foam placement for soil remediation, *Environ. Chem.* **14**(5), 338–343. <https://doi.org/10.1071/EN17003>

[Bertin et al., 1998] Bertin, H., Quintard, M. and Castanier, L. (eds): 1998, *Modeling Transient Foam Flow in Porous Media Using a Bubble Population Correlation*, Vol. All Days of *SPE Annual Technical Conference and Exhibition*, 27–30 September, New Orleans, Louisiana. SPE-49020-MS. <https://doi.org/10.2118/49020-MS>

[Birchak et al., 1974] Birchak, J., Gardner, C., Hipp, J. and Victor, J.: 1974, High dielectric constant microwave probes for sensing soil moisture, *Proceedings of the IEEE* **62**(1), 93–98.

[Bouزيد et al., 2018] Bouزيد, I., Maire, J., Ahmed, S. I. and Fatin-Rouge, N.: 2018, Enhanced remedial reagents delivery in unsaturated anisotropic soils using surfactant foam, *Chemosphere* **210**, 977–986. <https://www.sciencedirect.com/science/article/pii/S0045653518313390>

[Chang et al., 1990] Chang, S., Owusu, L., French, S. and Kovarik, F. (eds): 1990, *The Effect of Microscopic Heterogeneity on CO<sub>2</sub> -Foam Mobility: Part 2-Mechanistic Foam Simulation*, Vol. All Days of *SPE/DOE seventh Symposium on Enhanced Oil Recovery*, Tulsa, Oklahoma, 22–25 April. SPE-20191-MS. <https://doi.org/10.2118/20191-MS>

[Chavent, 1976] Chavent, G.: 1976, A new formulation of diphasic incompressible flows in porous media, in P. Germain and B. Nayroles (eds), *Applications of Methods of Functional Analysis to Problems in Mechanics*, Springer Berlin Heidelberg, Berlin, Heidelberg, pp. 258–270.

[Chen et al., 1999] Chen, J., Hopmans, J. and Grismer, M.: 1999, Parameter estimation of two-fluid capillary pressure-saturation and permeability functions, *Advances in Water Resources* **22**(5), 479–493. <https://www.sciencedirect.com/science/article/pii/S0309170898000256>

[Cheng et al., 2000] Cheng, L., Reme, A., Shan, D., Coombe, D., Rossen, W. et al.: 2000, Simulating foam processes at high and low foam qualities, *SPE/DOE Improved Oil Recovery Symposium*, Society of Petroleum Engineers.

[Choi et al., 2009] Choi, Y. J., Kim, Y.-J. and Nam, K.: 2009, Enhancement of aerobic biodegradation in an oxygen-limiting environment using a saponin-based microbubble suspension, *Environmental Pollution* **157**(8), 2197–2202. <https://www.sciencedirect.com/science/article/pii/S0269749109002073>

[Colombano et al., 2020] Colombano, S., Davarzani, H., van Hullebusch, E., Huguenot, D., Guyonnet, D., Deparis, J. and Ignatiadis, I.: 2020, Thermal and chemical enhanced recovery of heavy chlorinated organic compounds in saturated porous media: 1d cell drainage-imbibition experiments, *Science of The Total Environment* **706**, 135758. <https://www.sciencedirect.com/science/article/pii/S0048969719357535>

[Colombano et al., 2021] Colombano, S., Davarzani, H., van Hullebusch, E., Huguenot, D., Guyonnet, D., Deparis, J., Lion, F. and Ignatiadis, I.: 2021, Comparison of thermal and chemical enhanced recovery of DNAPL in saturated porous media: 2D tank pumping experiments and two-phase flow modelling, *Science of The Total Environment* **760**, 143958. <https://www.sciencedirect.com/science/article/pii/S0048969720374891>

[Couto et al., 2009] Couto, H. J., Massarani, G., Biscaia, E. C. and Sant'Anna, G. L.: 2009, Remediation of sandy soils using surfactant solutions and foams, *Journal of Hazardous Materials* **164**(2), 1325–1334. <https://www.sciencedirect.com/science/article/pii/S0304389408013848>

[Davarzani et al., 2021] Davarzani, H., Aranda, R., Colombano, S., Laurent, F. and Bertin, H.: 2021, Experimental study of foam propagation and stability in highly permeable porous media under lateral water flow: Diverting groundwater for application to soil remediation, *Journal of Contaminant Hydrology* **243**, 103917. <https://www.sciencedirect.com/science/article/pii/S016977222100156X>

[Davis and Sampson, 1986] Davis, J. C. and Sampson, R. J.: 1986, *Statistics and data analysis in geology*, Wiley New York et al.

[Delgado, 2007] Delgado, J.: 2007, Longitudinal and transverse dispersion in porous media, *Chemical Engineering Research and Design* **85**(9), 1245–1252. <https://www.sciencedirect.com/science/article/pii/S0263876207731635>

[Dholkawala et al., 2007] Dholkawala, Z., Sarma, H. and Kam, S.: 2007, Application of fractional flow theory to foams in porous media, *Journal of Petroleum Science and*

*Engineering* **57**(1-2), 152–165. Petroleum Exploration and Production Research in Australia.  
<http://www.sciencedirect.com/science/article/pii/S0920410506002208>

[Endres and Knight, 1992] Endres, A. I. and Knight, R.: 1992, A theoretical treatment of the effect of microscopic fluid distribution on the dielectric properties of partially saturated rocks, *Geophysical Prospecting* **40**(3), 307–324.  
<https://onlinelibrary.wiley.com/doi/abs/10.1111/j.1365-2478.1992.tb00377.x>

[Ettinger and Radke, 1992] Ettinger, R. A. and Radke, C. J.: 1992, Influence of Texture on Steady Foam Flow in Berea Sandstone, *SPE Reservoir Engineering* **7**(01), 83–90.  
<https://doi.org/10.2118/19688-PA>

[Falls et al., 1988] Falls, A., Hirasaki, G., Patzek, T. e. a., Gauglitz, D., Miller, D., Ratulowski, T. et al.: 1988, Development of a mechanistic foam simulator: the population balance and generation by snap-off, *SPE reservoir engineering* **3**(03), 884–892.

[Falls et al., 1989] Falls, A., Musters, J., Ratulowski, J. et al.: 1989, The apparent viscosity of foams in homogeneous bead packs, *SPE Reservoir Engineering* **4**(02), 155–164.

[Fergui et al., 1998] Fergui, O., Bertin, H. and Quintard, M.: 1998, Transient aqueous foam flow in porous media: experiments and modeling, *Journal of Petroleum Science and Engineering* **20**(1), 9–29.  
<https://www.sciencedirect.com/science/article/pii/S0920410598000369>

[Flores et al., 2011] Flores, G., Katsumi, T., Inui, T. and Kamon, M.: 2011, A simplified image analysis method to study LNAPL migration in porous media, *Soils and Foundations* **51**(5), 835–847.  
<https://www.sciencedirect.com/science/article/pii/S0038080620300895>

[Forey et al., 2021] Forey, N., Atteia, O., Omari, A. and Bertin, H.: 2021, Use of saponin foam reinforced with colloidal particles as an application to soil remediation: Experiments in a 2d tank, *Journal of Contaminant Hydrology* **238**, 103761.  
<https://www.sciencedirect.com/science/article/pii/S0169772220303508>

[Géraud et al., 2017] Géraud, B., Méheust, Y., Cantat, I. and Dollet, B.: 2017, Lamella division in a foam flowing through a two-dimensional porous medium: A model fragmentation process, *Phys. Rev. Lett.* **118**, 098003.  
<https://link.aps.org/doi/10.1103/PhysRevLett.118.098003>

[Glass and Nicholl, 1996] Glass, R. J. and Nicholl, M. J.: 1996, Physics of gravity fingering of immiscible fluids within porous media: An overview of current understanding and selected complicating factors, *Geoderma* **70**(2), 133–164.

[Glass et al., 1988] Glass, R., Steenhuis, T. and Parlange, J.-Y.: 1988, Wetting front instability as a rapid and far-reaching hydrologic process in the vadose zone, *Journal of Contaminant Hydrology* **3**(2), 207–226. Rapid and Far-Reaching Hydrologic Processes in the Vadose Zone. <https://www.sciencedirect.com/science/article/pii/0169772288900320>

[Glover, 2015] Glover, P.: 2015, 11.04 - geophysical properties of the near surface earth: Electrical properties, in G. Schubert (ed.), *Treatise on Geophysics (Second Edition)*, second edition edn, Elsevier, Oxford, pp. 89–137. <https://www.sciencedirect.com/science/article/pii/B9780444538024001895>

[Heimovaara et al., 1994] Heimovaara, T. J., Bouten, W. and Verstraten, J. M.: 1994, Frequency domain analysis of time domain reflectometry waveforms: 2. a four-component complex dielectric mixing model for soils, *Water Resources Research* **30**(2), 201–209. <https://agupubs.onlinelibrary.wiley.com/doi/abs/10.1029/93WR02949>

[Hematpur et al., 2018] Hematpur, H., Mahmood, S. M., Nasr, N. H. and Elraies, K. A.: 2018, Foam flow in porous media: Concepts, models and challenges, *Journal of Natural Gas Science and Engineering* **53**, 163–180. <https://www.sciencedirect.com/science/article/pii/S1875510018300878>

[Höhler and Cohen-Addad, 2005] Höhler, R. and Cohen-Addad, S.: 2005, Rheology of liquid foam, *Journal of Physics: Condensed Matter* **17**(41), R1041–R1069. <https://doi.org/10.1088/0953-8984/17/41/r01>

[Islam, 1988] Islam, M.R., F. A. S. (ed.): 1988, *Numerical Simulation Of Foam Flow In Porous Media*, Vol. All Days of *PETSOE Annual Technical Meeting*. PETSOE-88-39-04. <https://doi.org/10.2118/88-39-04>

[Jeong and Corapcioglu, 2003] Jeong, S.-W. and Corapcioglu, M. Y.: 2003, A micromodel analysis of factors influencing NAPL removal by surfactant foam flooding, *Journal of contaminant hydrology* **60**(1), 77–96.

[Kam, 2008] Kam, S. I.: 2008, Improved mechanistic foam simulation with foam catastrophe theory, *Colloids and Surfaces A: Physicochemical and Engineering Aspects* **318**(1-3), 62–77. <http://www.sciencedirect.com/science/article/pii/S0927775707010473>

[Kam et al., 2007] Kam, S. I., Nguyen, Q. P., Li, Q. and Rossen, W. R.: 2007, Dynamic Simulations With an Improved Model for Foam Generation, *SPE Journal* **12**(01), 35–48. <https://doi.org/10.2118/90938-PA>

[Kam and Rossen, 2003] Kam, S. I. and Rossen, W. R.: 2003, A Model for Foam Generation in Homogeneous Media, *SPE Journal* **8**(04), 417–425. <https://doi.org/10.2118/87334-PA>

[Kechavarzi et al., 2000] Kechavarzi, C., Soga, K. and Wiart, P.: 2000, Multispectral image analysis method to determine dynamic fluid saturation distribution in two-dimensional three-fluid phase flow laboratory experiments, *Journal of Contaminant Hydrology* **46**(3), 265–293. <https://www.sciencedirect.com/science/article/pii/S0169772200001339>

[Khatib et al., 1988] Khatib, Z., Hirasaki, G. and Falls, A.: 1988, Effects of Capillary Pressure on Coalescence and Phase Mobilities in Foams Flowing Through Porous Media, *SPE Reservoir Engineering* **3**(03), 919–926. <https://doi.org/10.2118/15442-PA>

[Kovscek and Bertin, 2003] Kovscek, A. R. and Bertin, H. J.: 2003, Foam mobility in heterogeneous porous media, *Transport in Porous Media* **52**(1), 37–49. <https://doi.org/10.1023/A:1022368228594>

[Kovscek and Radke, 1994] Kovscek, A. R. and Radke, C. J.: 1994, *Fundamentals of Foam Transport in Porous Media*, chapter 4, pp. 115–163. <http://pubs.acs.org/doi/abs/10.1021/ba-1994-0242.ch003>

[Lee, 2014] Lee, S.: 2014, *Modeling of Foam Flow in Porous Media for Subsurface Environmental Remediation*, PhD thesis, The University of Texas at Austin.

[Longpré-Girard et al., 2016] Longpré-Girard, M., Martel, R., Robert, T., Lefebvre, R. and Lauzon, J.-M.: 2016, 2d sandbox experiments of surfactant foams for mobility control and enhanced Inapl recovery in layered soils, *Journal of Contaminant Hydrology* **193**, 63–73. <https://www.sciencedirect.com/science/article/pii/S0169772216301826>

[Luciano et al., 2010] Luciano, A., Viotti, P. and Papini, M. P.: 2010, Laboratory investigation of DNAPL migration in porous media, *Journal of Hazardous Materials* **176**(1), 1006–1017. <https://www.sciencedirect.com/science/article/pii/S030438940901961X>

[Maire et al., 2019] Maire, J., Davarzani, H., Colombano, S. and Fatin-Rouge, N.: 2019, Targeted delivery of hydrogen for the bioremediation of aquifers contaminated by dissolved chlorinated compounds, *Environmental Pollution* **249**, 443–452. <https://www.sciencedirect.com/science/article/pii/S026974911834260X>

[Marfoe, 1987] Marfoe, C.H., K. H. R. W. (ed.): 1987, *Numerical Simulation of Foam Flow in Porous Media*, Vol. All Days of SPE Annual Technical Conference and Exhibition. SPE-16709-MS. <https://doi.org/10.2118/16709-MS>

[Millington and Quirk, 1961] Millington, R. J. and Quirk, J. P.: 1961, Permeability of porous solids, *Trans. Faraday Soc.* **57**, 1200–1207. <http://dx.doi.org/10.1039/TF9615701200>

[Mohammadi et al., 1995] Mohammadi, S., Collins, J. and A. Coombe, D.: 1995, Field application and simulation of foam for gas diversion. <https://www.earthdoc.org/content/papers/10.3997/2214-4609.201406964>

[Movchan et al., 2015] Movchan, T. G., Rusanov, A. I., Soboleva, I. V., Khlebunova, N. R., Plotnikova, E. V. and Shchekin, A. K.: 2015, Diffusion coefficients of ionic surfactants with different molecular structures in aqueous solutions, *Colloid Journal* **77**(4), 492–499. <https://doi.org/10.1134/S1061933X15040146>

[Mualem, 1976] Mualem, Y.: 1976, A new model for predicting the hydraulic conductivity of unsaturated porous media, water resource., *Water Resource Research* pp. 513 – 522.

[Myers and Radke, 2000] Myers, T. J. and Radke, C. J.: 2000, Transient foam displacement in the presence of residual oil: Experiment and simulation using a population-balance model, *Ind. Eng. Chem. Res.* **39**(8), 2725–2741. <https://doi.org/10.1021/ie990909u>

[O’Carroll et al., 2004] O’Carroll, D. M., Bradford, S. A. and Abriola, L. M.: 2004, Infiltration of PCE in a system containing spatial wettability variations, *Journal of Contaminant Hydrology* **73**(1), 39–63. <https://www.sciencedirect.com/science/article/pii/S0169772203002584>

[Omirebekov et al., 2020a] Omirebekov, S., Davarzani, H. and Ahmadi-Senichault, A.: 2020a, Experimental study of non-Newtonian behavior of foam flow in highly permeable porous media, *Industrial & Engineering Chemistry Research* **59**(27), 12568–12579. <https://doi.org/10.1021/acs.iecr.0c00879>

[Omirebekov et al., 2020b] Omirebekov, S., Davarzani, H., Colombano, S. and Ahmadi-Senichault, A.: 2020b, Experimental and numerical upscaling of foam flow in highly permeable porous media, *Advances in Water Resources* **146**, 103761. <https://www.sciencedirect.com/science/article/pii/S0309170820302074>

[Philippe et al., 2020] Philippe, N., Davarzani, H., Colombano, S., Dierick, M., Klein, P.-Y. and Marcoux, M.: 2020, Experimental study of the temperature effect on two-phase flow properties in highly permeable porous media: Application to the remediation of dense non-aqueous phase liquids (DNAPLs) in polluted soil, *Advances in Water Resources* **146**, 103783. <https://www.sciencedirect.com/science/article/pii/S0309170820301652>

[Philippe et al., 2021] Philippe, N., Davarzani, H., Colombano, S., Dierick, M., Klein, P.-Y. and Marcoux, M.: 2021, Experimental study of thermally enhanced recovery of high-viscosity DNAPL in saturated porous media under non-isothermal conditions, *Journal of Contaminant Hydrology* **243**, 103861. <https://www.sciencedirect.com/science/article/pii/S0169772221001005>

[Portois et al., 2018] Portois, C., Essouayed, E., Annable, M. D., Guiserix, N., Joubert, A. and Atteia, O.: 2018, Field demonstration of foam injection to confine a chlorinated solvent source zone, *Journal of Contaminant Hydrology* **214**, 16–23. <https://www.sciencedirect.com/science/article/pii/S0169772217303728>

[Rossen, 1990] Rossen, W. R.: 1990, Theory of mobilization pressure gradient of flowing foams in porous media, *Journal of Colloid and Interface Science* **136**(1), 1 – 16. <http://www.sciencedirect.com/science/article/pii/002197979090074X>

[Rossen et al., 1999] Rossen, W., Zeilinger, S., Shi, J. and Lim, M.: 1999, Simplified Mechanistic Simulation of Foam Processes in Porous Media, *SPE Journal* **4**(03), 279–287. <https://doi.org/10.2118/57678-PA>

[Rossen et al., 1994] Rossen, W., Zeilinger, S., Shi, J., Lim, M. et al.: 1994, Mechanistic simulation of foam processes in porous media, *SPE Annual Technical Conference and Exhibition*, Society of Petroleum Engineers.

[Roth and Attinger, 1990] Roth, K., S. R. F. H. and Attinger, W.: 1990, Calibration of time domain reflectometry for water content measurement using a composite dielectric approach, *Water Resources Research* **26**, 2267–2273.

[Schincariol et al., 1993] Schincariol, R. A., Herderick, E. E. and Schwartz, F. W.: 1993, On the application of image analysis to determine concentration distributions in laboratory experiments, *Journal of Contaminant Hydrology* **12**(3), 197–215. <https://www.sciencedirect.com/science/article/pii/016977229390007F>

[Shen et al., 2011] Shen, X., Zhao, L., Ding, Y., Liu, B., Zeng, H., Zhong, L. and Li, X.: 2011, Foam, a promising vehicle to deliver nanoparticles for vadose zone remediation, *Journal of Hazardous Materials* **186**(2), 1773–1780. <https://www.sciencedirect.com/science/article/pii/S0304389410016511>

[Stimson, 1974] Stimson, A.: 1974, *Photometry and radiometry for engineers*, Wiley, New York.

[Topp et al., 1980] Topp, G. C., Davis, J. L. and Annan, A. P.: 1980, Electromagnetic Determination of Soil Water Content, *Water Resources Research* **16**(3), 574–582.

[van Genuchten, 1980] van Genuchten, M. T.: 1980, A closed-form equation for predicting the hydraulic conductivity of unsaturated soils, *Soil Science Society of America Journal* **44**(5), 892–898. <https://access.onlinelibrary.wiley.com/doi/abs/10.2136/sssaj1980.03615995004400050002x>

[Wan et al., 2001] Wan, J., Veerapaneni, S., Gabelle, F. and Tokunaga, T. K.: 2001, Generation of stable microbubbles and their transport through porous media, *Water Resources Research* **37**(5), 1173–1182. <http://dx.doi.org/10.1029/2000WR900331>

[Wang and Beckermann, 1993] Wang, C.-Y. and Beckermann, C.: 1993, A two-phase mixture model of liquid-gas flow and heat transfer in capillary porous media-i. formulation, *International Journal of Heat and Mass Transfer* **36**(11), 2747–2758. <https://www.sciencedirect.com/science/article/pii/001793109390094M>

[Wang et al., 2012] Wang, J., Liu, H., Ning, Z. and Zhang, H.: 2012, Experimental research and quantitative characterization of nitrogen foam blocking characteristics, *Energy and Fuels* **26**(8), 5152–5163.

[Wang et al., 2017] Wang, Y., Liu, X., Bai, L. and Niu, J.: 2017, Influence of alkyl chain length of alpha olefin sulfonates on surface and interfacial properties, *Journal of Dispersion Science and Technology* **38**(12), 1764–1769. <https://doi.org/10.1080/01932691.2017.1281144>

[Wu et al., 2012] Wu, Y., Hubbard, S. and Wellman, D.: 2012, Geophysical monitoring of foam used to deliver remediation treatments within the vadose zone, *Vadose Zone Journal* **11**(4), vzj2011.0160. <https://access.onlinelibrary.wiley.com/doi/abs/10.2136/vzj2011.0160>

[Wu and Pruess, 2000] Wu, Y.-S. and Pruess, K.: 2000, Integral solutions for transient fluid flow through a porous medium with pressure-dependent permeability, *International Journal of Rock Mechanics and Mining Sciences* **37**(1), 51–61. <https://www.sciencedirect.com/science/article/pii/S136516099900091X>

[Zhang et al., 2009] Zhang, Z., Freedman, V. L. and Zhong, L.: 2009, *Foam transport in porous media: A review*, Pacific Northwest National Laboratory.

[Zhong et al., 2011] Zhong, L., Szecsody, J., Oostrom, M., Truex, M., Shen, X. and Li, X.: 2011, Enhanced remedial amendment delivery to subsurface using shear thinning fluid and aqueous foam, *Journal of Hazardous Materials* **191**(1-3), 249–257.

[Zhou et al., 1995] Zhou, Z., Rossen, W. et al.: 1995, Applying fractional-flow theory to foam processes at the " limiting capillary pressure", *SPE Advanced Technology Series* **3**(01), 154–162.